
Synchrotron X-Ray Phase Nanotomography for Bone Tissue Characterization

1

Peter Varga, Loriane Weber, Bernhard Hesse, and Max Langer

Contents

| | | |
|-----|---|----|
| 1 | Definition of the Topic | 2 |
| 2 | Overview | 2 |
| 3 | Introduction | 2 |
| 4 | Experimental and Instrumental Methodology | 5 |
| 4.1 | Instrumentation | 5 |
| 4.2 | Image Formation | 6 |
| 4.3 | Phase Retrieval | 10 |
| 5 | Key Research Findings | 12 |
| 5.1 | Literature Review: X-Ray Nano-tomography of Bone | 12 |
| 5.2 | Collagen Orientation | 18 |
| 5.3 | Morphology and FE Modelling of the Lacuno-Canalicular Network | 23 |
| 5.4 | Mineralisation on the Nanoscale | 27 |
| 6 | Conclusions and Future Perspective | 31 |
| 6.1 | Instrumentation | 31 |
| 6.2 | Bone Nano-imaging | 32 |
| | References | 33 |

P. Varga (✉)

Julius-Wolff-Institute & Berlin Brandenburg School for Regenerative Therapies,
Charité-Universitätsmedizin Berlin, Berlin, Germany

AO Research Institute Davos, Davos, Switzerland

e-mail: peter.varga@aofoundation.org

L. Weber • M. Langer

CREATIS, CNRS UMR5220, Inserm U1206, Université de Lyon, INSA-Lyon, Université Claude
Bernard Lyon 1, Villeurbanne, France

ESRF – The European Synchrotron, Grenoble, France

e-mail: loriane.weber@esrf.fr; max.langer@esrf.fr

B. Hesse

ESRF – The European Synchrotron, Grenoble, France

e-mail: bernhard.hesse@esrf.fr

© Springer-Verlag Berlin Heidelberg 2016

C.S.S.R. Kumar (ed.), *X-ray and Neutron Techniques for Nanomaterials
Characterization*, DOI 10.1007/978-3-662-48606-1_1

1

1 Definition of the Topic

X-ray phase nano-tomography allows the characterisation of bone ultrastructure: the lacuno-canalicular network, nanoscale mineralisation and the collagen orientation. In this chapter, we review the different X-ray imaging techniques capable of imaging the bone ultrastructure and then describe the work that has been done so far in nanoscale bone tissue characterisation using X-ray phase nano-tomography.

2 Overview

X-ray computed tomography at the micrometric scale is more and more considered as the reference technique in imaging of bone microstructure. The trend has been to push towards higher and higher resolution. Due to the difficulty of realising optics in the hard X-ray regime, the magnification has mainly been due to the use of visible light optics and indirect detection of the X-rays, which limits the attainable resolution with respect to the wavelength of the visible light used in detection. Recent developments in X-ray optics and instrumentation have allowed the implementation of several types of methods that achieve imaging limited in resolution by the X-ray wavelength, thus enabling computed tomography at the nanoscale. We review here the X-ray techniques with 3D imaging capability at the nanoscale: transmission X-ray microscopy, ptychography and in-line holography. Then, we present the experimental methodology for the in-line phase tomography, both at the instrumentation level and the physics behind this imaging technique. Further, we review the different ultrastructural features of bone that have so far been resolved and the applications that have been reported: imaging of the lacuno-canalicular network, direct analysis of collagen orientation, analysis of mineralisation on the nanoscale and the use of 3D images at the nanoscale as the basis of mechanical analyses. Finally, we discuss the issue of going beyond qualitative description to quantification of ultrastructural features.

3 Introduction

X-ray imaging and assessment of bone have been intimately linked already since the discovery of X-rays. Actually, the first application of X-rays was visualisation of bone on the organ level [1]. This consisted in simple projection images, usually known as radiographs. X-ray computed tomography (CT) [2, 3], that is, cross-sectional imaging, enables three-dimensional (3D) imaging by combining the acquisition of radiographs at several angles of rotation around the targeted object and a tomographic reconstruction algorithm. This modality has gained wide use in medical imaging. X-ray CT at the micron scale (μ CT) combines CT imaging with the use of high-resolution detectors. X-ray μ CT has recently assumed the place as the reference method for bone microstructure imaging, among other applications [4]. This is, apart from the excellent contrast in hard materials, sufficient penetration in bone and 3D

nature of the images, due to compact μ CT systems being increasingly available [5–7]. Synchrotron sources in combination with insertion devices are powerful X-ray sources enabling highly monochromatic X-rays. If such a source is used, the resulting modality is called synchrotron radiation μ CT (SR- μ CT) [8] that allows functional imaging, i.e. direct 3D quantification of the degree of mineralisation of bone (DMB) at the micro-scale [9].

The trend in μ CT and other X-ray microscopy techniques has been to go towards higher and higher resolution [10], since the properties of X-rays are very appealing: short wavelength (so a lower diffraction limit than with visible light) combined with high penetration power yielding good contrast in bone. This goes hand in hand with the increasing demand of quantitative 3D images of bone at the micro- and nano-scale, due to the links between ultrastructure and failure [11, 12]. The high penetration power makes it difficult to implement X-ray focusing optics, however, which has kept the magnification factor due to the X-ray beam fairly low. High-resolution imaging has instead been achieved by indirect detection: a fluorescent screen, a scintillator with a high efficiency in converting X-rays to visible light, imaged by standard visible light microscope optics onto a CCD camera [13]. This kind of system is diffraction limited in resolution by the wavelength of the visible light emitted by the scintillator, however. In this case, imaging of the ultrastructure cannot be considered, since this is usually reserved for features that are smaller than those resolvable with a standard bright field visible light microscope operating in transmission mode.

Osteoporosis and other bone fragility-related diseases are not yet fully understood and are thus the subject of active research. While previously the main focus was the characterisation, description and diagnosis of these diseases, currently the main aim is to uncover the mechanisms behind bone loss and those involved in bone failure. Bone mass is the most important determinant of bone strength, but it is known not to be the only factor. For example, collagen cross-linking is thought to be important for the integrity of the bone tissue [14]. Bone fragility is thought to result from failed material or structural adaptations to mechanical stress [15]. Since bone adapts to externally imposed mechanical stresses through a process of remodelling, the bone tissue changes its macro-, micro- and ultrastructure during its lifetime.

Bone remodelling is achieved via the processes of mechanosensation and mechanotransduction, which are thought to be performed by the osteocyte system. Osteocytes are the most abundant bone cells dispersed throughout the bone system. They differentiate from osteoblasts, which are the cells responsible for bone formation, by getting trapped in the pre-bone matrix during tissue formation. The osteocytes interconnect and communicate through dendritic processes [16–19]. The imprint of osteocytes and their processes are called the lacunae and the canaliculi, respectively, and form the lacuno-canalicular network (LCN) [20]. The sensitivity of osteocytes to external strain could be due to sensing substrate deformation directly or by strains induced by the flow of interstitial fluid circulating in the LCN [21–23]. Moreover, microcracks are also thought to trigger remodelling by interrupting osteocyte dendrites [24–27]. The interest in studying osteocytes and their pore network has been on the rise the last few years, which can be witnessed by

published statements such that the LCN is “the unrecognized side of bone tissue” or that osteocytes “can’t hide forever” [28–32]. Apart from their presumed role in the bone remodelling, these cells are also thought to contribute to the maintenance of mineral homeostasis. In relation to this, they secrete a number of biochemical factors, of which some are seen as potential therapeutic targets [33]. It should be mentioned however that the complete role of the osteocyte, and other possible processes for bone remodelling, is not yet fully elucidated but is rather the topic of active research [34].

Osteocytes and the LCN are not the only aspects of bone ultrastructure that are interesting to study, however. At the ultrastructural level, bone tissue is a natural nanocomposite consisting of mineralised collagen fibres. These fibres are organised in a regular fashion around the vessel canals: the Haversian canals forming the centre in units of bone remodelling called osteons and Volkmann canals interconnecting the Haversian canals and the periosteum. During the lifetime of bone tissue, mineralised matrix is being resorbed by osteoclasts and replaced by osteoblasts with new osteons. Between these secondary osteons, there remain rests of older tissue called interstitial tissue. At the boundary of each osteon, there is a layer of mineralised tissue called the cement line, which is thought to have an important role in limiting crack propagation and to affect the overall stiffness of bone [35, 36]. The cement line has previously been characterised mainly using quantitative backscatter electron imaging (qBEI). It has been disputed whether the cement line is hypo-mineralised [35, 36] or hyper-mineralised [37, 38]. It may also act as a boundary of the interconnected porosity within an osteon. At least one study has reported canalicular tunnelling through the cement line, however [39].

The organisation of the collagen fibrils is thought to directly influence bone strength and toughness. The analysis of collagen orientation has so far been performed mainly in 2D using scanning electron microscopy [40–43], transmission electron microscopy [44] and atomic force microscopy [45] or indirectly analysed by polarised light microscopy [46] and Raman spectral mapping [47, 48]. So far very little data is available on the 3D fine structure of the LCN and the bone matrix on the nanoscale. X-ray μ CT has been used extensively to study bone tissue microstructure. There has been some work performed on imaging the LCN using μ CT [49–55]. Since the diameter of the canaliculi can be as small as ~ 100 nm, μ CT cannot by definition be used to image ultrastructure however, as mentioned above.

The techniques used to image bone ultrastructure in 3D have so far been transmission electron microscopy, scanning electron microscopy and confocal laser scanning microscopy (CLSM). CLSM is however limited by the depth of penetration in mineralised tissue, and its spatial resolution is anisotropic, depending on the depth into the sample where the focus is placed. It is also a scanning technique, which implies that data acquisition is relatively slow. Finally, advanced staining and sample preparation is necessary [56].

Another technique which has recently been progressing towards chemical imaging of bone ultrastructure is infrared nanoscopy. Even though this technique gives only access to the chemical properties in 2D, it might be of increasing interest due to

the increasing number of available instruments, relatively simple sample preparation and high spatial resolution up to tens of nm at a field of view in the order of $100 \times 100 \mu\text{m}$ [57, 58].

Serial sectioning using a focused ion beam followed by imaging with scanning electron microscopy (FIB-SEM) to image the lacuno-canalicular network has been reported [42, 43, 59, 60]. While this technique offers excellent spatial resolution, it is a destructive technique, and it requires advanced sample preparation. The repeated sectioning and imaging also lead to long acquisition times. Finally, transmission electron tomography has been used to image osteocyte ultrastructure in situ [61]. However, this kind of imaging is limited to very thin sections, $3 \mu\text{m}$ in the cited work. Thus, the 3D information is quite limited and only provides a very local visualisation of the osteocyte.

We review here the work that has been done in imaging of the ultrastructure of bone in 3D using X-rays. We give a brief introduction to high-resolution X-ray imaging physics. We then continue to describe the different imaging methods that have been used for ultrastructural imaging in bone, along with the results that were obtained. We give particular attention to the propagation-based technique, where we outline more in detail the image formation and reconstruction. We then describe the type of analyses that have so far been possible at shorter length scales than can be seen by visible light. Finally, we briefly discuss what we consider the next step of 3D ultrastructure imaging in bone: the possibility of in situ cell imaging in bone using X-ray phase nano-tomography.

4 Experimental and Instrumental Methodology

4.1 Instrumentation

4.1.1 X-Ray Source

The work described in Sects. 5.1.3, 5.2, 5.3 and 5.4 was performed on beamline ID22 at the European Synchrotron Radiation Facility (ESRF), Grenoble, France. ID22 is located on a high- β straight section and was equipped with two insertion devices: an in-vacuum U23 and a revolver U35/U19. The electron beam in the synchrotron had a current of ~ 200 mA, an energy of 6 GeV and a relative energy spread of 0.001. The vertical (horizontal) emittance, β values and dispersion were 39 pm (3.9 nm), 3 m (37.2 m) and 0 m (0.137 m), respectively. The revolver device was chosen to give maximum photon output in a moderately narrow energy range centred on 17.5 keV, which is the principal working energy for imaging at ID22 [62].

4.1.2 X-Ray Optics

The X-ray focusing optics consisted of two graded multilayer coated mirrors mounted in a crossed Kirkpatrick-Baez (KB) configuration [63]. The vertical mirror was 112 mm long and had a focusing distance of 180 mm, and the horizontal mirror was 76 mm long and had a focusing distance of 83 mm. The mirrors were

dynamically bendable to create the appropriate elliptical shape required to focus the X-ray beam. The resulting reflectivity at 17 keV was 73 % and yielded a spot size of approximately $50 \text{ nm} \times 50 \text{ nm}$. The vertical mirror images directly the undulator source ($\sim 25 \text{ }\mu\text{m}$ FWHM), whereas in the horizontal direction, a virtual source is created by the use of high heat-load slits. The multilayer mirrors both focus and monochromatise the beam, resulting in a very high flux of about 5×10^{12} photons/s and a moderate degree of monochromaticity of $\Delta E/E \approx 10^{-2}$ [64–68].

4.2 Image Formation

The refractive index n of an object can be described as [69]:

$$n(x, y, z) = 1 - \delta(x, y, z) + i\beta(x, y, z), \quad (1.1)$$

where δ is the refractive index decrement, related to the phase shift of the incident wave after passing through the sample, and β is the absorption index, related to the attenuation of the incident beam induced by the sample.

The refractive index decrement δ and the absorption index β can be respectively expressed as [69]

$$\delta = \frac{r_c \lambda^2}{2\pi} \rho_e \quad (1.2)$$

and

$$\beta = \frac{r_c \lambda^3 \rho_e}{4\pi^2 c} \sum_j \frac{f_j \gamma_j}{Z}, \quad (1.3)$$

where r_c denotes the classical electron radius, λ the wavelength of the X-ray beam, ρ_e the electron density, c the light velocity, f_j the number of electrons per atom with damping constant γ_j and Z the atomic number that corresponds to the total number of electrons per atom. Here, j corresponds to an electron in the atom.

The absorption index β is related to the attenuation coefficient μ by the following relationship [70]:

$$\mu(x, y) = \frac{4\pi}{\lambda} \int \beta(x, y, z) dz. \quad (1.4)$$

The attenuation B and phase shift φ induced by the object can be described as projections parallel to the propagation direction (here, the z -axis). Note that \mathbf{x} represents the vector (x, y) .

$$B(\mathbf{x}) = \frac{2\pi}{\lambda} \int \beta(\mathbf{x}, z) dz \quad (1.5)$$

and

$$\varphi(\mathbf{x}) = -\frac{2\pi}{\lambda} \int \delta(\mathbf{x}, z) dz. \quad (1.6)$$

At each angle θ , the interaction between the object and the X-ray wave can be described as a transmittance function:

$$T_\theta(\mathbf{x}) = \exp(-B_\theta(\mathbf{x}) + i\varphi_\theta(\mathbf{x})). \quad (1.7)$$

Thus, if $u_{\text{inc}}(\mathbf{x})$ denotes the incident wave front and $u_0(\mathbf{x})$ the wave front right after the sample (i.e. for a null propagation distance), we obtain

$$u_0(\mathbf{x}) = T_\theta(\mathbf{x})u_{\text{inc}}(\mathbf{x}). \quad (1.8)$$

The corresponding intensity recorded by the detector, without any propagation, is

$$I_0(\mathbf{x}) = |u_0(\mathbf{x})|^2 \quad (1.9)$$

$$I_0(\mathbf{x}) = |T_\theta(\mathbf{x})u_{\text{inc}}(\mathbf{x})|^2 \quad (1.10)$$

$$I_0(\mathbf{x}) = |e^{-B_\theta(\mathbf{x})} e^{i\varphi_\theta(\mathbf{x})} u_{\text{inc}}(\mathbf{x})|^2 = |e^{-B_\theta(\mathbf{x})}|^2 |e^{i\varphi_\theta(\mathbf{x})}|^2 |u_{\text{inc}}(\mathbf{x})|^2 \quad (1.11)$$

$$I_0(\mathbf{x}) = e^{-2B_\theta(\mathbf{x})} |u_{\text{inc}}(\mathbf{x})|^2 = e^{-2B_\theta(\mathbf{x})} I_{\text{inc}}(\mathbf{x}). \quad (1.12)$$

The free-space propagation over a distance D can be modelled by the Fresnel transform involving the propagator P_D [71]:

$$P_D(\mathbf{x}) = \frac{1}{i\lambda D} \exp\left(i\frac{\pi}{\lambda D} |\mathbf{x}|^2\right) \quad (1.13)$$

and its Fourier transform:

$$\tilde{P}_D(\mathbf{f}) = \exp\left(-i\pi\lambda D |\mathbf{f}|^2\right), \quad (1.14)$$

where $\mathbf{f} = (f, g)$ are the conjugate variables corresponding to \mathbf{x} .

Usually, in computer implementations, the propagator is applied in the Fourier domain, since there it becomes a multiplication instead of a convolution in the spatial domain. Mathematically, if $u_0(\mathbf{x})$ and $u_D(\mathbf{x})$ respectively denote the wave fronts right after the sample and at a distance D from the sample, we obtain

$$u_D(\mathbf{x}) = P_D(\mathbf{x}) * u_0(\mathbf{x}), \quad (1.15)$$

in the spatial domain, which corresponds to

$$\tilde{u}_D(\mathbf{f}) = \tilde{P}_D(\mathbf{f})\tilde{u}_0(\mathbf{f}) \quad (1.16)$$

in the Fourier domain.

Since u_D usually stays in the real domain, and the propagator is applied in the Fourier domain, we get

$$u_D(\mathbf{x}) = \mathcal{F}^{-1}\tilde{P}_D\mathcal{F}[u_0](\mathbf{x}). \quad (1.17)$$

The operator

$$\mathcal{F}r_D = \mathcal{F}^{-1}\tilde{P}_D\mathcal{F} \quad (1.18)$$

is called the Fresnel transform. If we assume flat illumination, the interaction between the incident wave front and the sample followed by free-space propagation over a distance D can be modelled by

$$T_{\theta,D}(\mathbf{x}) = (T_{\theta} * P_D)(\mathbf{x}). \quad (1.19)$$

The intensity recorded by the detector at a distance D is

$$I_{\theta,D}(\mathbf{x}) = |T_{\theta,D}(\mathbf{x})|^2. \quad (1.20)$$

In the Fourier domain, the intensity can be expressed as

$$\tilde{I}_D(\mathbf{f}) = \int T\left(\mathbf{x} - \frac{\lambda D\mathbf{f}}{2}\right) T^*\left(\mathbf{x} + \frac{\lambda D\mathbf{f}}{2}\right) \exp(-i2\pi\mathbf{x} \cdot \mathbf{f}) d\mathbf{x}. \quad (1.21)$$

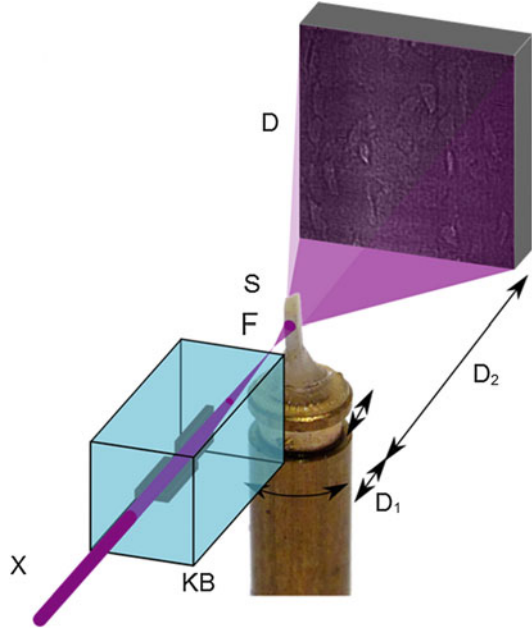
Thus, images recorded by the detector are quantitatively related to the phase shift of the wave induced by the object.

Holotomography consists in acquiring projections for a complete rotation of the sample, at different sample-to-detector distances. This enables to cover well the Fourier domain (the Fresnel transform can have zero crossing at certain distances).

4.2.1 Magnified Images Formation

Since the beam is divergent, recording an image at sample-to-detector distance D also induces, apart from phase contrast, magnification of the projections and creates a spherical wave front (Fig. 1.1). The magnification M is expressed using the well-known Thales' theorem:

Fig. 1.1 The incoming parallel X-ray beam (X) is focused onto a focal spot (F) using Kirkpatrick-Baez mirrors, curved reflective optics that will horizontally and vertically focus the beam. D_1 represents the distance between the spot (F) and the sample (S). D_2 denotes the propagation distance, i.e. the distance between the sample and the detector [72]



$$M = \frac{D_1 + D_2}{D_1}. \quad (1.22)$$

We obtain projections with different magnification by modifying the propagation distance. In practice, the detector and the focus point are fixed, i.e. $D_1 + D_2$ is constant. It means that it is the sample that moves along a translation stage to get images with different magnifications.

Note that the spherical wave Fresnel diffraction phenomenon can be seen as a plane-wave illumination problem at the defocusing distance D defined by

$$\begin{aligned} \frac{1}{D} &= \frac{1}{D_1} + \frac{1}{D_2} \\ \leftrightarrow D &= \frac{D_1 D_2}{D_1 + D_2} \\ \leftrightarrow D &= \frac{D_2}{M}. \end{aligned} \quad (1.23)$$

In the following, D denotes the defocusing distance and can be seen as an equivalent of the propagation distance that takes into account the magnification.

Since the position of the focus and the detector are kept fixed, $[D_1, D_2, D_n, \dots, D_N]$ represents the equivalent propagation distance indexed by n , with N the total number of distances used.

4.3 Phase Retrieval

4.3.1 Contrast Transfer Function

To retrieve the phase information from the image recorded by the detector (which is a non-linear problem), and since we are in the Fresnel diffraction regime, we can use the contrast transfer function (CTF) model. This linear model, which expresses the intensity as a linear function of the absorption and the refractive index decrement, is valid for slowly varying phase and weakly absorbing objects. These two conditions can be mathematically written as

$$|\varphi(\mathbf{x}) - \varphi(\mathbf{x} + \lambda D\mathbf{f})| \ll 1 \quad (1.24)$$

for slowly varying phase and

$$B(\mathbf{x}) \ll 1 \quad (1.25)$$

for weak absorption.

The CTF is based on the linearisation of the transmittance function to the first order:

$$T(\mathbf{x}) \approx 1 - B(\mathbf{x}) + i\varphi(\mathbf{x}). \quad (1.26)$$

By substituting the linearisation of the transmittance function in Eq. 1.21 and keeping only the first-order terms, we get the CTF:

$$\tilde{I}_D(\mathbf{f}) = \delta_{\text{Dirac}}(\mathbf{f}) - 2 \cos(\pi\lambda D|\mathbf{f}|^2) \tilde{B}(\mathbf{f}) + 2 \sin(\pi\lambda D|\mathbf{f}|^2) \tilde{\varphi}(\mathbf{f}), \quad (1.27)$$

Where \sim denotes the Fourier transform and δ_{Delta} the Dirac delta function.

Nevertheless, for nano-tomography, the propagation distances are relatively long compared to the pixel size and wavelength. This means the condition in Eq. 1.24 and thus the linearisation in Eq. 1.26 are no longer valid, so that the non-linear contribution of the phase cannot be neglected [73].

The CTF can be rewritten to take this into account:

$$\tilde{I}_D(\mathbf{f}) = \delta_{\text{Dirac}}(\mathbf{f}) - 2 \cos(\pi\lambda D|\mathbf{f}|^2) \tilde{B}(\mathbf{f}) + 2 \sin(\pi\lambda D|\mathbf{f}|^2) \tilde{\varphi}(\mathbf{f}) + \tilde{I}_{\text{NL},D}(\mathbf{f}), \quad (1.28)$$

where $\tilde{I}_{\text{NL},D}(\mathbf{f})$ represents the non-linear contribution.

Phase retrieval is thus performed in two stages. An initial guess of the phase is determined using a classical linear least square minimisation using the CTF, described in Sect. 4.3.2. This first guess corresponds to the linear part of the retrieved phase, but is not sufficient to provide good image quality at such high resolution. After, the non-linear term is determined using a non-linear iterative method, for example, a non-linear conjugate gradient algorithm [72].

4.3.2 Phase Retrieval with the CTF

To retrieve the phase using the CTF, linear least square optimisation is used. This method is usually used to solve an overdetermined problem, for example, a problem containing one unknown and N equations, as it is the case here, since we recorded images at N distances (that constitute our N equations) and want to determine one unknown, the phase.

Consider the following overdetermined problem:

$$y_n = A_n x + \varepsilon_n, \quad (1.29)$$

where n is an integer so that $n \in [1 : N]$, x is the unknown, y_n denotes one of the N measurements and A_n is the linear transformation applied to x to get y_n . The linear least square method determines an estimate of x , \hat{x} , so that

$$\frac{1}{N} \sum_{n=1}^N A_n^2 \hat{x} = \frac{1}{N} \sum_{n=1}^N A_n y_n. \quad (1.30)$$

Solving CTF (Eq. 1.27) is equivalent to minimise

$$\sum_{n=1}^N \left| 2 \sin(\pi \lambda D_n |\mathbf{f}|^2) \tilde{\varphi}(\mathbf{f}) - 2 \cos(\pi \lambda D_n |\mathbf{f}|^2) \tilde{\mathbf{B}}(\mathbf{f}) - \tilde{I}_{D_n}(\mathbf{f}) \right|^2. \quad (1.31)$$

Here, Tikhonov regularisation is used to solve this minimisation problem [74]:

$$\hat{\varphi}(\mathbf{f}) = \frac{\left[K_{aa} \sum_{n=1}^N 2 \sin(\pi \lambda D_n |\mathbf{f}|^2) \tilde{I}_{D_n}(\mathbf{f}) - K_{ap} \sum_{n=1}^N 2 \cos(\pi \lambda D_n |\mathbf{f}|^2) \tilde{I}_{D_n}(\mathbf{f}) \right]}{K_{aa} K_{pp} - K_{ap}^2} \quad (1.32)$$

with

$$K_{aa} = \sum_{n=1}^N \left(2 \cos(\pi \lambda D_n |\mathbf{f}|^2) \right)^2 \quad (1.33)$$

$$K_{ap} = \sum_{n=1}^N 2 \cos(\pi \lambda D_n |\mathbf{f}|^2) 2 \sin(\pi \lambda D_n |\mathbf{f}|^2) \quad (1.34)$$

$$K_{pp} = \sum_{n=1}^N \left(2 \sin(\pi \lambda D_n |\mathbf{f}|^2) \right)^2. \quad (1.35)$$

Once the projections are well conditioned, phase retrieval is performed according to the scheme presented above. A linear least square method is performed to assess roughly the phase and a non-linear conjugate gradient method to refine it. The obtained phase projections are eventually used as an input of a tomographic reconstruction algorithm (here, the filtered back projection method) to get a volume of the refractive index decrement.

5 Key Research Findings

5.1 Literature Review: X-Ray Nano-tomography of Bone

We review here the imaging methods that have so far been used to image bone ultrastructure at higher than 400 nm spatial resolution and the results that were obtained. To achieve such resolutions, advanced X-ray microscopy methods have to be used, where some magnification has to be implemented on the X-ray beam. This is not straightforward, however, as mentioned above, since the very small deviation from unity of the refractive index for X-rays makes it difficult to implement X-ray optics. The methods are surprisingly heterogeneous in their design, relying on attenuation and far-field and near-field diffraction, respectively.

5.1.1 Ptychographic Tomography

One way to achieve high-resolution imaging with X-rays is to exploit diffraction. This requires the use of a pencil beam, either by using a pinhole or X-ray focusing optics. An image is then recorded at a relatively long distance downstream of the object, which corresponds to far-field or Fraunhofer diffraction. Images recorded in this way will contain information closely related to the squared modulus of the Fourier transform of the imaged object, convolved with the Fourier transform of the incident beam. It is in certain cases possible to reconstruct the object transmission function by the use of iterative phase retrieval algorithms based on projections onto sets [75–78]. This approach is usually known as coherent diffraction imaging (CDI) [79, 80]. Since the recorded image is in the frequency domain, the attainable resolution is limited by how far from the centre of the detector signal can be measured (and, of course, the wavelength of the probe). In practice, this means that the resolution limit is related to the signal-to-noise ratio in the recorded images. Therefore, very high resolution can be achieved with this technique. CDI is limited to imaging of isolated particles with a support smaller than the used X-ray beam, however, such as isolated nanoparticles [82] or single cells [83].

The small support requirement can be obviated by scanning the probe across an extended sample while letting the probe position overlap at each image position (in practice the sample is scanned through the beam). By using an iterative reconstruction scheme, a complete phase projection can be reconstructed [84–86]. This is known as ptychographic imaging [87].

Since the phase shift introduced by the object in the X-ray beam can be considered as a straight-line projection, if we have access to the phase shift, we can use it to reconstruct the 3D refractive index decrement distribution in the sample, in analogy to the classical attenuation case. What is particularly attractive with this is that for hard X-rays, the refractive index decrement is proportional to the local mass density in the sample [88]. This means that, for example, the use of X-ray phase tomography images to drive mechanical simulations avoids the need to infer the mass density from measurements of the degree of mineralisation of bone (DMB), which has to be done if density is to be related to the attenuation index [9]. In practice, phase tomography is implemented by a two-step process: first, the phase is retrieved at

each projection angle, and then the refractive index decrement is reconstructed by feeding the resulting phase maps into a tomographic reconstruction algorithm such as filtered back projection (FBP) [89–91].

Ptychographic tomography has been used to image bone ultrastructure [81]. A human cortical bone sample cut to an approximately cylindrical shape with a diameter of $\sim 25 \mu\text{m}$ was imaged using a $2.3 \mu\text{m}$ pinhole (Fig. 1.2a). The sample was scanned through the resulting pencil beam so that the X-ray spots lie on concentric circles, covering a rectangular area of $40 \mu\text{m} \times 32 \mu\text{m}$ (Fig. 1.2b) for a total of 704 diffraction patterns per projection. Such projections were recorded over a 180° turn of the sample, at increments of 1° for a total of 180 projections.

Figure 1.2c, d shows virtual sections through the reconstructed electron density map. The bright shell on the surface of the sample is due to the sample preparation; the sample was cut using a focused ion beam, which deposits a residue of heavy ions on the surface (in this case gallium ions). We can easily see the lacunae and the canaliculi. Note that the reported electron densities are truly quantitative due to the sample being completely covered by the projections. 3D renderings (Fig. 1.2e, f) show that the imaged volume contains three partial lacunae. The canaliculi are fairly well resolved, but some spurious structures remain.

The major strength of ptychographic tomography is that it is capable of attaining very high resolutions without the use of X-ray optics. Isotropic 3D resolutions up to 16 nm have been reported [92], however, in energy ranges that are probably too low to be practical for bone imaging ($\sim 6 \text{ keV}$). A major drawback of ptychographic tomography is its scanning nature. This makes the acquisition time for a single projection relatively long; in practice, it limits the number of projections that can be acquired and the field of view that can be covered. In the work of Dierolf et al. [81], only 180 angular positions were acquired, normally far too few to achieve correct angular resolution, and a relatively small sample was imaged, comprising only parts of three lacunae. The duration of the complete acquisition was reported to be $\sim 40 \text{ h}$. Another disadvantage, shared with the in-line phase imaging (Sect. 5.1.3), is that reconstruction is not always straightforward. Considerable expertise seems to be needed to perform correct reconstructions. These two drawbacks taken together seem to limit the applicability of ptychographic tomography for quantitative studies. Additionally, ptychography can only reconstruct phase shifts in the range 0 – 2π . This means that if the true phase shift is larger than 2π , the reconstruction has to be unwrapped, which is a problem unto itself [93].

5.1.2 Transmission X-Ray Microscopy (TXM)

Magnification on the X-ray side can be achieved by the implementation of a transmission X-ray microscope, analogously to what can be done with visible light. Due to the weak refraction of X-rays, diffractive optics, so-called Fresnel zone plates, are used for this purpose. A full-field TXM implementation has been reported by Andrews et al. [94], using either a rotating anode X-ray source or a synchrotron source to image bone tissue at the nanoscale. They used a reflective capillary collimator due to its high focusing efficiency. The sample was placed in the focus. A Fresnel zone plate was used as objective lens to image the beam onto the

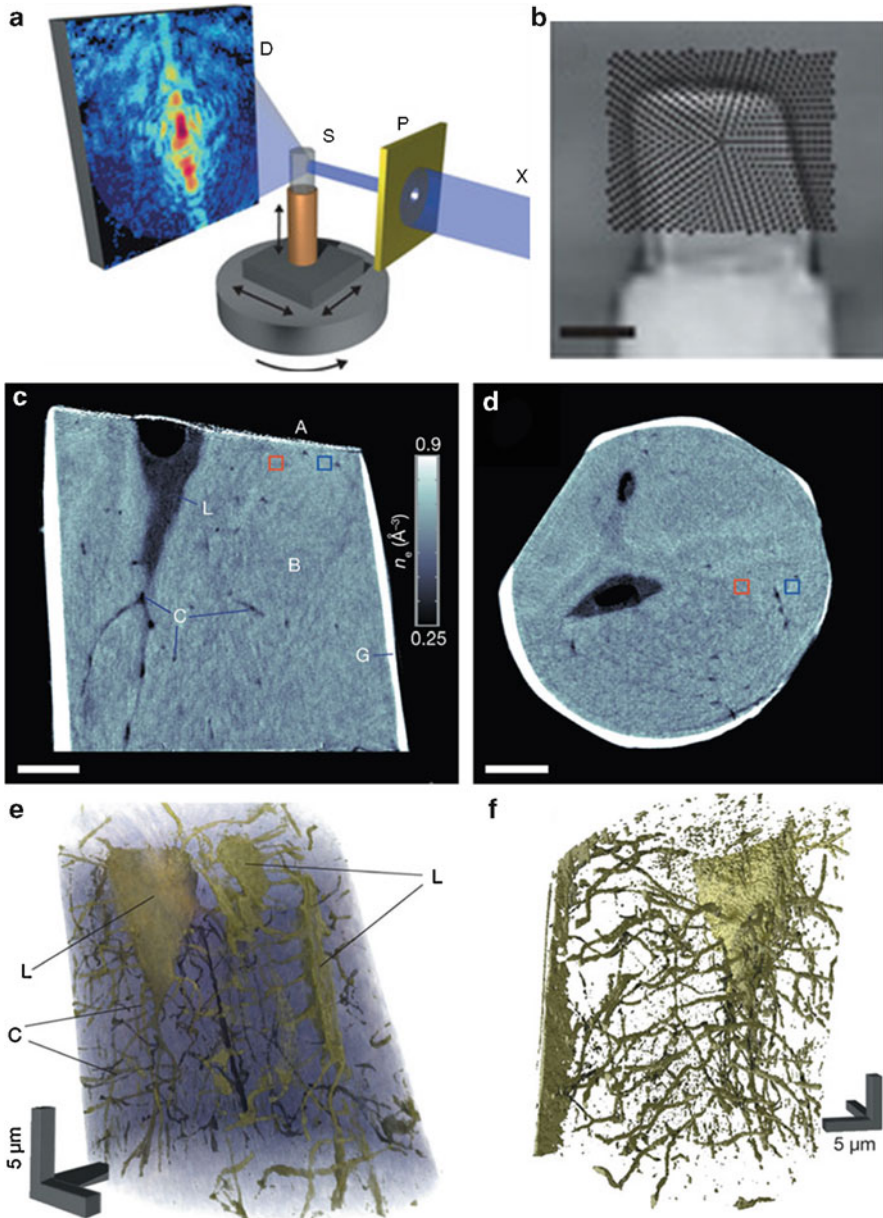


Fig. 1.2 Ptychographic X-ray tomography. (a) Schematic of the experimental setup. (b) The scanning pattern of the X-ray spot over the sample to form one projection. (c, d) Virtual cuts through the reconstructed volume showing very good contrast between bone and the LCN. The bright shell consists of gallium ions deposited by the focused ion beam cutting of the sample. (e) Volume rendering of the complete imaged volume. Three lacunae can be partially seen, and a fair amount of the canaliculi seem well resolved. (f) Zoom on one lacuna and its canaliculi. A fair amount of spurious porosity remains (Images from Dierolf et al. [81])

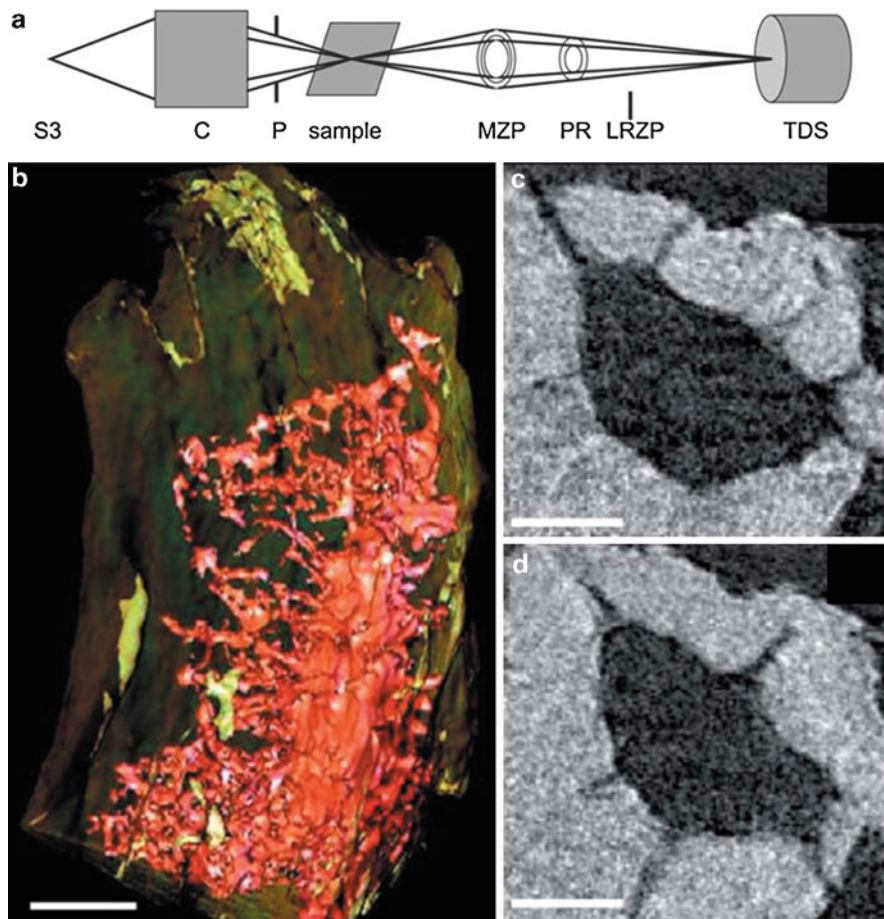


Fig. 1.3 Transmission X-ray microscopy (TXM). (a) Schematic of the experimental setup. (b) Volume rendering of an osteocyte lacuna in an isolated murine trabecula. (c, d) Virtual cuts through the reconstructed volume showing the contrast between bone, the lacuna and the canaliculi (Images from Andrews et al. [94])

detector. Detection was done using a scintillator-based high-resolution CCD camera with a physical pixel size of $\sim 2 \mu\text{m}$. A schematic of the instrument is shown in Fig. 1.3a. The X-ray energy used was in the range of 4–14 keV. They achieved a spatial resolution of $\sim 50 \text{ nm}$, compared to the theoretical resolution limit of $\sim 35 \text{ nm}$.

The reported TXM setup was used to image the LCN. Part of one lacuna and its envioning canaliculi were imaged in trabecular bone. The sample was extracted from the proximal region of a mouse tibia by microtome cutting, followed by washing with a saline jet to remove marrow. It was then dried and attached to a steel cannula tip with epoxy for imaging. The resulting sample consisted of a single trabecula and was less than $50 \mu\text{m}$ thick, which is approximately the depth of focus

of the TXM. The sample was stained with 1 % uranyl acetate for 12 h to improve contrast. The lacuna and canaliculi are well resolved in the image, but are fairly weakly contrasted (Fig. 1.3c, d). Looking at a volume rendering (Fig. 1.3b), the lacuna and its canaliculi are clearly visible. The canaliculi show a surprising rate of branching, however, compared to the two other techniques reported here.

A TXM images the attenuation of the sample, i.e. the same contrast as in standard X-ray μ CT. An advantage of TXM is that it can achieve high spatial resolution without the need for advanced image reconstruction. The disadvantages seem to be the demanding sample preparation and the limited sample size due to the short depth of field, approximately 50 μ m. The technique also requires fairly low energies, thereby limiting the thickness of the samples that can be traversed. The lower energy also increases the X-ray dose deposited in the sample, thus increasing the risk of radiation damage.

5.1.3 In-line Phase Tomography

It is possible to implement a transmission projection microscope by the use of X-ray optics to focus the beam and placing the sample after the focus in the resulting divergent beam. This kind of microscope has been implemented using Kirkpatrick-Baez reflective optics [95]. As for the methods discussed above, the sample is placed on a translation/rotation stage to enable tomographic imaging. The camera is mounted on a translation stage to allow for different factors of geometrical magnification. The magnification is a function of the beam divergence after the focus, the focus-to-sample distance and the focus-to-detector distance. The resulting free-space propagation not only creates a magnification effect however, but due to the high degree of coherence of the beam, phase contrast is also induced. This contrast can be used to reconstruct the phase shift in the object. One particularity, however, is that the recorded images will lack information at certain spatial frequencies due to the properties of the transfer function of the Fresnel propagator. In high-resolution imaging, this makes it necessary to acquire several (at least two) images per projection angle, corresponding to different sample-to-detector distances. Another aspect is that bone samples will always introduce a considerable attenuation effect at the energies used in practice. This means that both attenuation and phase contrast will be present in the recorded images, which also imposes a minimum of two images per projection angle. Otherwise, strong assumptions have to be made on the sample composition to make phase retrieval possible.

The phase can be retrieved at each projection angle by a process known as phase retrieval. Several algorithms for phase retrieval from Fresnel diffraction patterns have been developed. Most of them are based on linearisation of the squared modulus of the Fresnel transform to achieve efficient, filtering-based solutions [89, 90, 96–99]. In the high-resolution case, there will be non-negligible non-linear contributions. This makes the use of non-linear reconstruction algorithms necessary to achieve the resolution permitted by the experimental setup (Sect. 4.3) [100–104].

In-line phase tomography has been used to image several ultrastructural features in bone [72]. The LCN can be imaged over a relatively large field of view (Fig. 1.4a–d). The LCN also seems better resolved than then in the previously

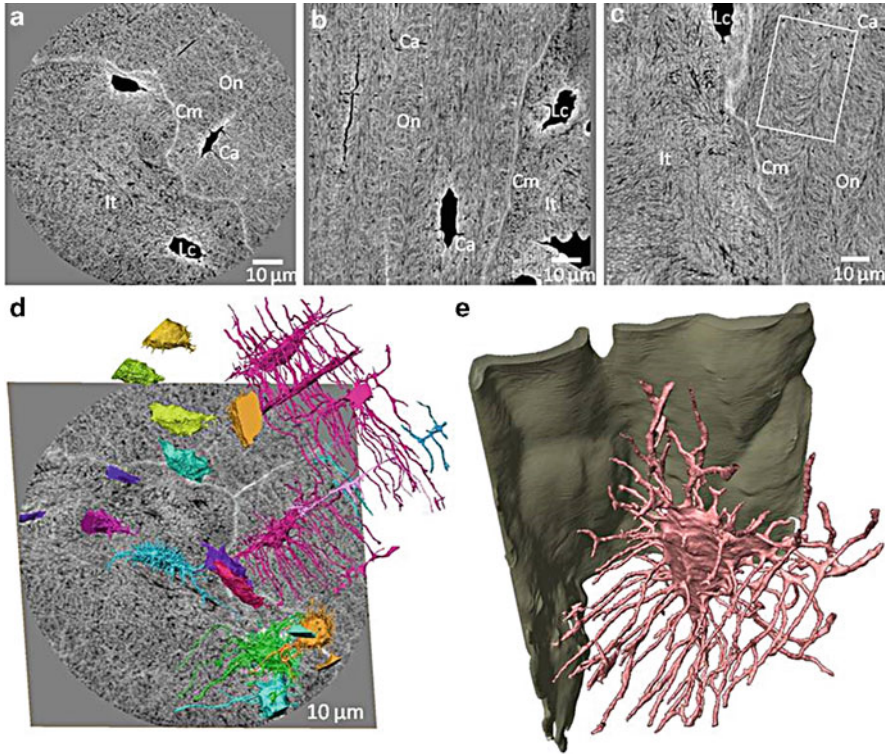


Fig. 1.4 Magnified phase tomography of bone. (a–c) Virtual cuts through the reconstructed volume. Note the high contrast between the LCN and the bone matrix and also the strong contrast in the matrix presumably due to oblique cutting of the mineralised collagen fibres, as well as the well-resolved cement line. (d) Volume rendering of all LCN porosity in the sample showing a relatively large number of lacunae. (e) Zoom on one lacuna and its canaliculi (*pink*) and the cement line (*green*). The LCN is rendered in unprecedented detail, and its relationship to the cement line can be studied [72]

reported studies (cf. Figs. 1.2f, 1.3b and 1.4e). The bone matrix appears strongly textured (Fig. 1.4a–c) compared to, e.g. images acquired with X-ray ptychographic tomography (Fig. 1.2c–d). By comparison to qBEI [40] and TEM [44] images, the arching structure can be identified to be due to the oblique cutting of the mineralised collagen fibrils. This means that the collagen fibre orientation can be studied directly in 3D using texture analysis, as we will see below. The cement lines are comparatively very well contrasted. In phase tomography, the reconstructed grey level corresponds to the mass density in non-hydrogen-rich materials. In the images, it can be seen that the cement line has a significantly higher mass density than the surrounding osteonal and interstitial tissue regions.

In-line phase tomography has some aspects that make it attractive for bone imaging. It is a full-field imaging technique, which means that the image acquisition is relatively fast. Acquisition time of ~4 h per sample has been reported [72], using

full sets of projections (i.e. 3000 projections using a 2048-element-wide detector). This means that quantitative studies on large series of samples are potentially within the capabilities of this technique. Further, due to the full-field nature, a relatively large field of view can be imaged compared to the other available techniques.

The in-line technique currently has one disadvantage in common with ptychographic tomography, however. Image reconstruction is not straightforward, since it relies on advanced reconstruction algorithms that presently require considerable expertise to operate. A disadvantage compared to ptychography is currently the achievable spatial resolution. While no measurement has been reported, by inspection of the reconstructed volumes, the spatial resolution so far achieved seems to be ~ 200 nm (FWHM at interfaces in the reconstructed 3D object). With these advantages and disadvantages taken together, in-line phase tomography seems to be an appropriate method for quantitative studies and study of ultrastructural features in addition to the LCN.

5.2 Collagen Orientation

Three-dimensional images acquired by means of in-line phase tomography allow to explore the details of the submicron-scale architecture of bone. In particular, the structure of bone lamellae can be analysed in unprecedented detail.

Lamellar pattern is the dominating arrangement of bone in the human skeleton and can be found most frequently in the form of osteons. Osteons are approximately 200 μm diameter cylindrical structural units constituted by concentrically arranged lamellae surrounding the central Haversian canal of 50–100 μm diameter hosting blood vessels and nerves. Lamellae are 3–7 μm thick layers that were characterised and defined originally on microscopy images of cut sections. The reason for the appearance of lamellae was already more than hundred years ago proposed to be the ultrastructure, namely, the orientation of the collagen-mineral composite [105].

One interesting question has been – and still is – if the lamellar structure is the result of a collagen self-assembly processes [44, 106] or if it is determined by the activity of the osteoblasts laying down bone tissue, driven through their mechanosensing ability, following a predefined programme or signals sent by osteocytes. However, the major driving force behind studies investigating bone microarchitecture has been the role of these structural details in determining function and vice versa. Ultimately, in-depth knowledge on structure–function relationships may complete our understating of the complex design and remarkable mechanical properties of these highly optimised skeletal elements [107]. The effect of bone diseases on the mechanical competence and the underlying alterations in the composition and architecture are also of great interest. Moreover, the underlying principles may be useful for the design of new materials for mimicking bone tissue [106] or for other bio-inspired engineering purposes.

With respect to the role of ultrastructure in mechanical properties of lamellar bone, besides numerous other studies, the works of Ascenzi and colleagues have to be mentioned. These authors extensively researched and reported the potential

relationships between the osteonal types classified based on appearance under confocal microscopy and mechanical properties of isolated osteons [108–111] and lamellae [111] assessed experimentally. However, understanding the exact architecture of lamellar bone remained a challenging task mainly due to the available tools of investigation. Inference of the three-dimensional arrangement of collagen fibrils and/or mineral particles was attempted from 2D sections acquired mainly by various microscopy techniques [109, 112–119], scattering [120–122] and diffraction based [123], i.e. mainly in reflection or transmission mode. Interpretation of these results therefore required assumptions and theoretical models. Some of these approaches lead to partially or fully misleading conclusions as it was pointed out, e.g. by Giraud-Guille et al. [112]. Using these various methods, several researchers' opinion converged towards the agreement that lamellae have a periodic plywood structure. However, various descriptive models have been proposed including orthogonal [105], twisted [112], rotated [114] and helicoidal [124] plywoods. Furthermore, a remarkably different opinion was formulated by Marotti et al. [125], proposing that the collagen matrix is rather disorganised and the lamellar pattern is the result of neighbouring regions having distinct collagen densities. A potential explanation for these different observations has been provided recently [126]. However, there was a clear need for truly three-dimensional analysis techniques to fully resolve these structural details and explain the partially or fully contradicting findings of previous 2D analyses.

In-line phase tomography provides the density contrast and spatial resolution that are sufficient to investigate and quantitatively describe this complex arrangement in three dimensions.

As pointed out in Sect. 5.1.3, the characteristic arcing pattern apparent in Fig. 1.4a–c is the result of this lamellar structure and was an important basis for previous 2D, e.g. electron microscopy-based analyses attempting to resolve the lamellar structure [112]. Having the 3D data at hand, it is possible to virtually prepare slices in arbitrary directions. Aligning these slices with the lamellar plane allows one to observe the arrangement of collagen fibrils within sub-lamellae. This principle was the basis of the image analysis protocol presented in [127]. In particular, slice-wise autocorrelation analysis was performed to quantify the local orientation of the fibrils. We assumed that the in-plane pattern of the fibrils was quasi-periodic and used the major principal axis of the autocorrelation-based orientation distribution function of periodicity to identify the dominant direction of fibrils within the given plane. Independently assessed results of consecutive parallel slices provided the evolution of the mean orientation of the bone lamellae. Several sub-volumes aligned with the local lamellar coordinate system were investigated.

Using this technique, we confirmed that mineralised collagen fibrils in lamellar bone are organised into a plywood structure that is made of parallel quasi-planes in which the fibrils have unidirectional alignment. Within the largest analysed region, having an in-lamellar-plane dimension of approximately $30 \times 70 \mu\text{m}$, the standard deviation of the quantified fibril orientation was as small as five degrees. The evolution of fibril orientation across lamellae was dominated by smooth transitions; discrete changes were rare. We found two major plywood pattern types. The first one

resembled the rotating plywood described earlier [112], with the orientation changing continuously. For the first time, to our knowledge, we quantified the rate of twist and found that it was fairly constant across regions and specimens, being approximately $25^\circ/\mu\text{m}$. The range of twist was close to either 180° or 360° . Fibrils completed a 180° twist in approximately $7\ \mu\text{m}$, which corresponds well with lamellar thickness values reported earlier [128]. In the second lamellar type, the change of fibril orientation followed a closely sinusoidal pattern, with average amplitude of approximately 30° and a relatively small offset, on average seven degrees, around the osteon axis. We called this pattern oscillating plywood and found cases resembling symmetric as well as rather asymmetric sinusoids. The average half period of these sinusoids was close to six microns, which is again close to previously reported lamellar thickness values. This pattern was close to that found earlier [123] in a single sample, however, with a much smaller offset with respect to the osteon axis.

We found twisting and oscillating plywood patterns to coexist within the same osteon in a consecutive manner. Close to the external boundary of the osteon, i.e. at the cement line, we observed in all investigated cases twisting plywood arrangement. The lamellar structure of osteons was hypothesised to have importance mechanically by acting as an efficient crack arresting boundary and thus protect the vessels and nerves within the central canal [107]. Our finding is in line with this hypothesis as twisted plywood contains all fibril orientations and, by means of collagen bridging, may therefore be a general defensive mechanism against cracks in any direction [129] and it is located directly at the external border of the osteon. Furthermore, the outermost lamella, being the firstly deposited one, may be important in the early phase of the construction of the osteon.

As a qualitative validation of our approach, in a selected analysis region, the computed orientation was used to construct a virtual 3D fibril model that compared well with the corresponding sub-volume of the original greyscale image, and, in particular, the arch pattern could be reproduced (Fig. 1.5). The figure illustrates the necessity of 3D analysis as the evaluated complex arrangement displayed in the centre panel of Fig. 1.5 cannot be retrieved from a 2D section, e.g. from the oblique cut shown in the left panel.

Apart from the plywood-type arrangements, we could observe rather disorganised regions [130]; however, these had very rare occurrence. Furthermore, we found that fibrillar orientation was independent of the local mass density values, suggesting that the known fluctuation of mechanical properties across lamellae [117, 131–133] is dominated by the orientation of the fibrils rather than the level of mineralisation.

In summary, our results not only corroborated findings of earlier studies, but provided novel insight into the lamellar microstructure in bone. Further, a unique set of quantitative results could be derived from nanoscale three-dimensional data and allowed reinterpretation of previous observations. Moreover, our findings were in line with the results of the concurrent, but independently performed, studies of Reznikov et al. investigating lamellar arrangement in various species by means of FIB-SEM [42, 60, 134]. This approach is attractive as it provides a resolution of about $10\ \text{nm}$. However, it is limited to a field of view of $10\ \mu\text{m}$ and at the price of full destruction of the sample. Finally, the existence of the two plywood arrangements

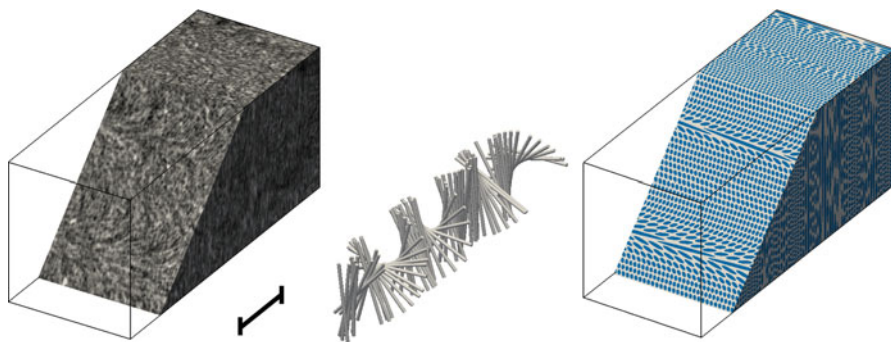


Fig. 1.5 Qualitative validation of the autocorrelation-based approach to quantify mineralised collagen fibril orientation. *Left*: rectangular analysis volume cropped from the synchrotron nano-CT image of a human femoral cortical bone sample with an oblique cut. Grey values represent the inverted mass density in arbitrary units. Scale bar, 10 μm . *Middle*: cylinders representing the quantified fibril orientation of 600 μm thick sections across the lamellae. *Right*: 3D illustration of the extracted orientations with the fibrils shown in blue and the matrix in white. The arc pattern in the oblique cut corresponds well to that in the original image (*left*) [127]

was corroborated in a later study using polarised Raman microscopy for the chemical and structural analysis of human osteonal bone [48].

Nevertheless, the analysis method developed and applied in [127] had several limitations, since:

- (i) Its application was restricted to large osteons in which the curvature of lamellae was relatively small, allowing to have a rectangular ROI with slices that contained data of distinct lamellar quasi-planes and that were large enough for the extraction of the orientation.
- (ii) The analysis region had to be aligned with the local lamellar planes, which required time-consuming manual preprocessing (image rotation, ROI selection).
- (iii) The analysis regions had to be located sufficiently far away from osteocyte lacunae, and fibril orientation around these pores could not be assessed.

Most of these limitations can be overcome by employing a truly 3D approach. The lamellar arrangement consists of planes with unidirectional fibrils, orientation of which changes relatively rapidly across the lamellae. This direction-dependent rate of the orientation change requires the analysis method to be well tuned to this structure. The updated analysis protocol has two steps. In the first one, the rough lamellar orientation is assessed, which is used in a second step to align the rectangular analysis volume. The size of the latter, to be in accordance with the above discussed closely transversely isotropic orientation change rate, is larger in the lamellar plane than out of this plane. The capabilities of this approach are illustrated in Fig. 1.6 which shows the quantified fibril orientation around an osteocyte lacuna. In comparison to the previous method, the improved analysis protocol requires much

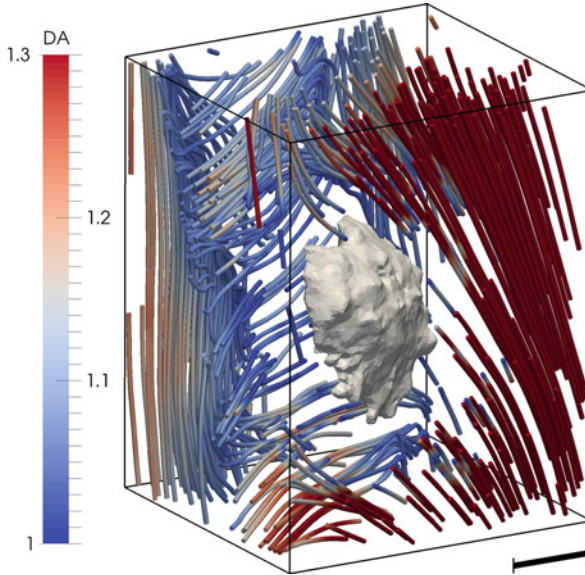


Fig. 1.6 Illustration of the mineralised collagen fibril orientation around an osteocyte lacuna, as estimated by the updated 3D autocorrelation-based approach. The lacuna is shown as *white* surface in the *middle* of the rectangular volume. Colour of the cylinders represents the degree of anisotropy (*DA*) of the autocorrelation-based measure, i.e. the fidelity of the orientation estimation. On the *left side* of the lacuna, the orientation may have abrupt changes from closely vertical to horizontal. However, the low *DA* values suggest that fibrils are rather disorganised in this region. Scale bar, 5 μm

less user interaction, essentially limited to the selection of the volume of interest. Moreover, as shown in the figure, the region does not have to be aligned with the lamellar plane and can include larger voids such as lacunae. Therefore, the new approach is expected to allow for high-throughput analyses, which is a strong requirement in, e.g. comparative studies with several groups and larger sample sizes.

A rather general limitation of all high-resolution methods is the strong sampling effect due to the available field of view. This effect can be compensated by scanning multiple regions of the same sample and/or increasing the number of specimens to strengthen statistical power. The expected improvements in imaging technology should provide the basis for larger, even clinically relevant studies. However, the relatively low accessibility of the infrastructure remains a challenge. In this respect, the role of coarser-scale methods that are sensitive to the alteration of the lamellar structure or the fluctuations of its mechanical properties has to be emphasised. More easily accessible laboratory techniques such as scanning acoustic microscopy [117], Raman microscopy [48] or second harmonic imaging [135, 136] have been demonstrated for this purpose. Moreover, these methods allow for the investigation of larger domains, however, only in 2D. These approaches may therefore efficiently complement the higher-resolution 3D techniques, and their combination should open new possibilities towards more extensive studies in the future.

5.3 Morphology and FE Modelling of the Lacuno-Canalicular Network

Porosity of bone is at least as important as the mineralised tissue matrix itself, both biologically and mechanically. On the micro-scale of cortical bone, one finds the pore network of osteocytes that consists of the lacunae hosting the cell bodies and the canaliculi, which are tiny tunnels connecting lacunae of neighbouring cells [11, 137]. Given the important role of the mechanosensitive osteocyte in the coordination of the activities of other bone cells and its active participation in remodelling [29, 138], the LCN has received increasing attention during the last years. Imaging of this pore network became an important, but not yet fully solved, challenge [11, 139].

Osteocyte lacunae are ellipsoidal-shaped voids in the bone matrix with approximate sizes of $5\ \mu\text{m} \times 10\ \mu\text{m} \times 20\ \mu\text{m}$ and can therefore be resolved with laboratory devices such as confocal microscopy and desktop μCT [11, 12, 140]. Nevertheless, most studies used μCT in combination with a synchrotron source to image lacunae and quantify their morphology [49, 53, 54, 141–143]. Not only the morphology of lacunae [12, 53, 144] but also that of the entire LCN including the canaliculi has been reported to be altered in different bone diseases [145].

The connection between lacunae provided by the canalicular network is essential due to several reasons. Osteocyte dendrites can extend in these tunnels and connect to the neighbouring cell via gap junctions, allowing for direct communication [146]. Even more importantly, this network is filled with interstitial fluid which is in motion due to changes in blood pressure and to deformations caused by mechanical loading of bones [147]. Fluid flow transports nutrients, removes cell waste and distributes signalling molecules. The latter are important in the biochemical control of bone remodelling.

Nevertheless, the remodelling process is driven also by mechanical signals to which these cells are also sensitive [31]. There is increasing evidence that motion of this liquid may stimulate osteocytes by deforming the membrane of the cell body or the dendrites [148, 149] or the primary cilia [150]. However, these processes are not yet fully understood, and fluid flow may not be the source of or may not be the only mechanism of triggering osteocytes to initiate remodelling. Direct straining through the deformation of the surrounding extracellular matrix may be an alternative or additional means for mechanical stimulation of osteocytes [151].

An unresolved issue with respect to both previous theories is the order of magnitude difference between the strains available in vivo (few thousand microstrains) [152] and the one required to stimulate these cells in vitro (few tens of thousands of microstrains) [153], giving rise to a missing strain amplification mechanism. This phenomenon has received increased attention during the last years and has been researched using experimental [154], analytical [149, 153, 155, 156] and numerical [22, 23, 157–162] approaches. In-depth analysis of the potential relevance of the pore network of osteocytes in bone diseases and in remodelling in general requires appropriate description of the geometry and 3D architecture of the entire LCN including the canaliculi. This task is far more challenging than imaging

of the lacunar pores described above, mainly due to the tiny dimensions of these canals embedded in the dense mineralised tissue.

The repertoire of the available appropriate experimental tools is very restricted; the available data is limited and shows high deviations for certain quantitative descriptors of the LCN [137, 163]. Scanning electron microscopy-based studies of Marotti et al. reported canalicular diameter to be between 150 and 500 nm [164], but 3D analysis is not possible with this method. The network properties of LCN can be investigated based on confocal microscopy images [56, 165–167], but detailed description of the canal geometry is not possible since the resolution of this method is practically the same as the average canalicular diameter, i.e. approximately 300 nm. The same is true for attenuation-based synchrotron tomography [54, 55].

Higher-resolution imaging can be achieved by means of the FIB-SEM approach [59], ptychography [81] or tomographic transmission electron microscopy [61]. However, these methods are expensive in terms of time and resources and provide a relatively small field of view; and FIB-SEM is fully destructive. In-line phase tomography can overcome some of these limitations by providing very high spatial resolution in a relatively large field of view within reasonable image acquisition time (Sect. 5.1.3). We used this technique to reconstruct the geometrical details of the LCN and investigate a potential means of mechanical stimulus of osteocytes [168].

In that study, the in-line phase tomography protocol described above (Sect. 5.1.3) was used to image cylindrical samples of human femoral cortical bone. Sample preparation was challenging since cylindrical samples with diameter less than 700 μm had to be prepared from several specimens within a relatively short time and with reasonable costs. We used a precision lathe for this purpose. First, a few mm wide and deep and approximately 15–20 mm long rods were cut, by means of a diamond-coated wheel saw, from a prescribed location of the femoral cortical cross sections. These samples were then mounted on the lathe using custom-built holders, and the required sample diameter was achieved by careful turning. This protocol allowed to preserve the close to native state of the samples. However, the resulting bone cylinders had to be dried prior to scanning to avoid potential sample motion during image acquisition.

Imaging provided us with an overview image with 715 μm field of view containing the entire cross section of the cylinders with 350 nm voxel size and a high-resolution image of selected regions with 102 μm field of view and 50 nm voxel size. Rectangular volumes of interest (VOIs) were selected from the high-resolution images to analyse the LCN and deformations of osteocytes. Each VOI contained a single lacuna with its canaliculi (Fig. 1.7a).

First, the geometry of the pores was identified using specialised segmentation methods including thresholding, morphological operations and a custom-developed connectivity enhancement algorithm. The latter was required to correct the effects of ring artefacts artificially cutting some canaliculi. In each VOI, the lacuna was then separated from the canaliculi, and several morphological parameters of both pore compartments were quantified (Fig. 1.7b). These included volumes, surfaces, descriptors of shape as well as number, diameter and spacing of canaliculi.

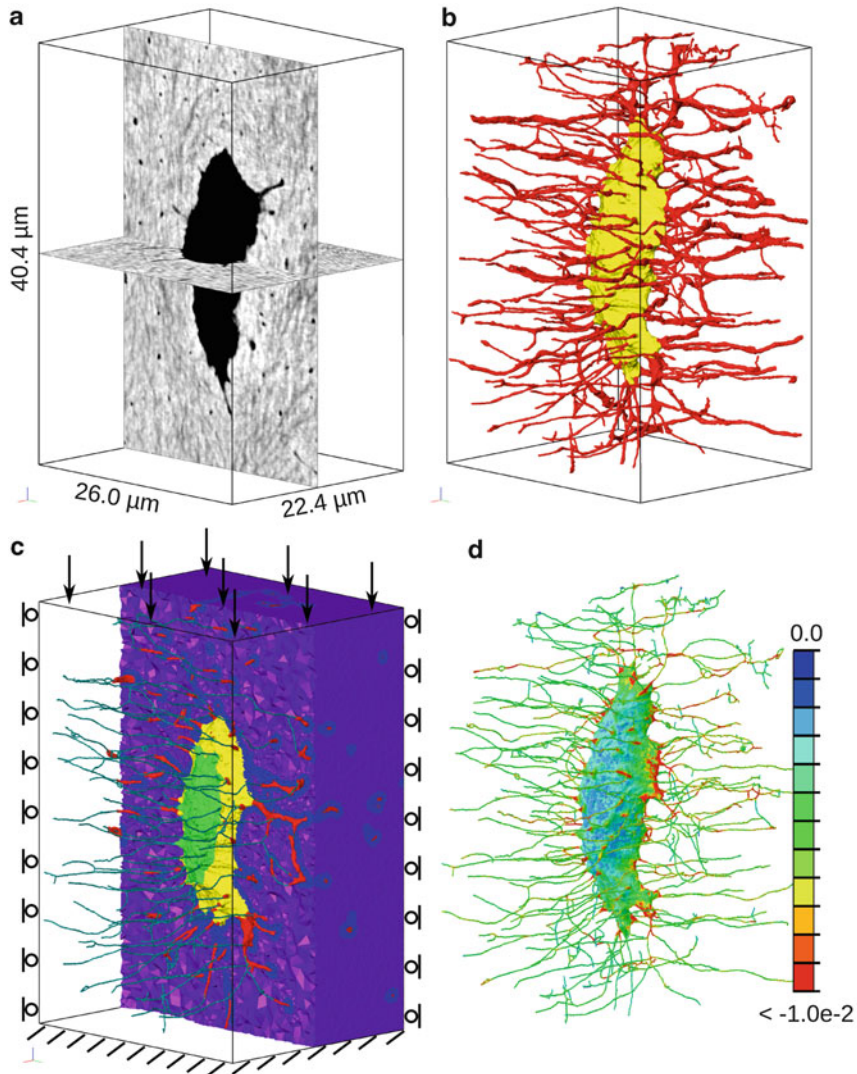


Fig. 1.7 Quantification of lacunar-canalicular morphology and prediction of osteocyte strains. (a) Selected VOIs from phase nano-CT images of femoral cortical bone of a 66-year-old female donor. Grey values represent the mass density. (b) Surface rendering of the segmented lacunar (yellow) and canalicular (red) pores. (c) Finite element mesh containing the mineralised extracellular matrix (purple and blue), the pericellular soft tissue in the lacuna (yellow) and in the canaliculi (red), as well as the cell body (light green) and processes (turquoise), with both the latter reconstructed artificially based on literature data. Parts of the model are transparent to allow visualisation of all compartments. Boundary conditions applied in the deformation analysis, i.e. constrained uniaxial compression of 1000 microstrains, are also shown. (d) Minimum (compressive) principal strain results of the finite element analysis in the osteocyte, showing deformation peaks (red, >10,000 microstrains; i.e. an at least tenfold strain amplification) at the junctions of the dendrites and cell body as well as at certain locations of the dendrites further away from the lacuna [168]

Case-specific finite element models of the VOIs were created from the same images. These models included the extracellular matrix surrounding the pores, the pericellular soft tissue matrix in the lacuna and the canaliculi as well as the osteocyte with its cell body and dendrites (Fig. 1.7c). As the cell itself was not visible on the images, assumptions based on previous literature data collected with electron microscopy imaging [160, 169] were used to artificially reconstruct its geometry from the available pore-matrix interface data. Moreover, each canaliculus was assumed to contain a cell dendrite. Material properties were modelled as linear elastic and isotropic, with parameters assigned based on literature data [22]. The models were subjected to confined uniaxial compressive deformation along the direction of the longest lacunar dimension with magnitude set to the physiologically relevant 1000 microstrains [152].

In-line phase tomography imaging provided unprecedented details of the LCN (Fig. 1.7). The most important results of the quantitative morphological analysis of the ten investigated regions of interest were as follows. The lacunar volume (min, $342 \mu\text{m}^3$; max, $686 \mu\text{m}^3$), surface (min, $295 \mu\text{m}^2$; max, $503 \mu\text{m}^2$) and aspect ratio of the approximating ellipsoid (min, 2.0; max, 4.8) varied considerably between the investigated VOIs. Lacunae located at the outer border of the osteons, i.e. in the direct vicinity of the cement lines were less elongated than others. Average canalicular diameter was comparable among different VOIs (min, $0.29 \mu\text{m}$; max, $0.44 \mu\text{m}$), but the number of canaliculi per lacuna (min, 53; max, 126), as well as the total volume (min, 2.4×10^{-3} ; max, 9.3×10^{-3}) and surface area (min, $23 \times 10^{-3} \mu\text{m}^{-1}$; max, $84 \times 10^3 \mu\text{m}^{-1}$) of canaliculi, with both latter being normalised bone volume, showed higher variations. However, average distance between the canaliculi was found to fall into a relatively narrow range (min, $4.3 \mu\text{m}$; max, $5.1 \mu\text{m}$). This finding, in combination with the correlation between canalicular number and lacunar surface area ($R = 0.79$), suggested that the spatial distribution of canaliculi was very well regulated. Within the VOIs, the volume of canaliculi was 2–9 times smaller than that of the lacuna, but their surface area was 1.3–4.5 times larger. These results, although limited by the VOI-based analysis, underlined the potential of these pores in the interaction with the matrix.

The main outcome of the finite element analysis was that the magnitude of the strains at the junctions of the osteocyte cell body and dendrites reached up to 70 times the externally applied deformations and further local peaks were observed in the dendrites (Fig. 1.7d). Resulting strain magnitudes are in the range reported to stimulate osteocytes *in vitro* [153]. These findings provide a potential explanation of the sought strain amplification effect described above. The case-specific models predicted higher strain amplification factors compared not only to idealised ones [157–159] but also to previously reported case-specific simulations using either different image source [22] or less refined modelling approach [162].

However, these high strains were localised in a very small portion on the cell volume. There was no evident relation between the cell deformation and the parameters of the LCN morphology of the investigated osteocytes. One of the derived deformation-related parameters, the relative dendrite volume in which the strain amplification was higher than tenfold, was similar in the VOIs originating

from the same bone sample – and practically the same osteon – in two out of three cases. This suggests that local tissue age, even if not considering the related increase in the mineralisation and consequently in the stiffness of the extracellular matrix, may have an impact on osteocyte deformations.

Our analyses were limited by the number of investigated osteocytes. Future studies should therefore include several samples from numerous donors so that appropriate statistical analyses can be performed. The automated analysis protocol presented in [168] provides the efficiency required for such large-scale studies. Moreover, the effect of bone diseases on LCN morphology and osteocyte deformations could be investigated with the above described tools.

A further main limitation was the fact that the cells were not visible in the nano-CT images and thus had to be reconstructed artificially using literature-based data and a priori assumptions. However, recent advances in imaging technology are providing very high contrast and spatial resolution. This contrast may provide the possibility of imaging not only the mineralised matrix but also the cell itself in situ. Promising results in this respect have been achieved by means of both ptychography and in-line phase tomography. Moreover, the ultra-high resolution of these methods may allow to examine unprecedented details of osteocytes and their connection to the mineralised wall. Particularly interesting in this respect would be the focal adhesions of the cell dendrites to the canalicular wall [149, 169] as these were reported to be highly sensitive to mechanical stimuli [170]. However, conservation of the in vivo-like conditions of the cells would still remain a challenge for these imaging experiments [169].

Direct straining is just one of the potential theories for mechanical stimulation of osteocytes. Fluid flow-induced stimuli may indeed be of key importance in this respect. The potential of this theory, demonstrated analytically [149] and numerically [23], may be further refined with the aid of 3D spatial description of the pericellular space and the adhesion sites of osteocytes. Advances in imaging are expected to provide important details also to these models and ultimately the answer to the still not fully resolved phenomenon of osteocyte mechanosensation.

5.4 Mineralisation on the Nanoscale

Phase-contrast-based X-ray imaging techniques at the nanoscale allow to gain new insight into mineral exchange at the interface between the osteocyte network and the surrounding mineralised matrix for human bone tissue. The findings summarised in this section suggest that spatial distribution of bone tissue mass density is determined by the canalicular network morphology.

Bone is a biological material structured hierarchically over several length scales, from the molecular level of collagen to the organ level [107, 171]. Mechanical properties of bone depend on its composition and structure at all length scales. However, structural support is only one of the functions of bones; their role as mineral storage has been receiving attention recently. On the way towards

understanding the latter, details on the morphology of the micro(n) porosity as well as the properties of the surrounding mineralised tissue at this scale became of high interest.

In bone remodelling, maturation of the newly formed osteonal bone tissue is associated with a rapid primary increase in mineralisation followed by a slower secondary phase. This increase in mineralisation requires supply and precipitation of minerals into the bone matrix. Mineral delivery can occur only from the extracellular fluid via interfaces such as the Haversian system and the osteocyte pore network.

After the process of rapid initial mineralisation, a secondary mineralisation process takes place, which adds about 10 % more mineral over a period of several years [172]. In [172] it is also outlined that an average turnover of about 12 % per year at a total body calcium of 1000 g and a bone loss of about 1 % per year leads to a net calcium flux of about 30 mg out of an adult skeleton each day. However, much larger fluxes of calcium between the extracellular fluid (ECF) and the bone matrix have been reported than could be explained through osteoblast/osteoclast activity [172–174].

It is believed that the calcium concentration in the ECF is controlled mainly by the parathyroid hormone (PTH) [175], a non-collagenous protein. This study also reports that it is via PTH that the concentration of calcium in the ECF is elevated from the basic level of 35 mg/l to the required physiological level of 50 mg/l. Excess mineral ions are limited by the renal threshold for calcium which has to be coordinated with the processes of mineral exchange at the ECF-bone matrix interface by PTH. A large amount (~90 %) of the ECF-bone interface is made up by the lacuna-canalicular surface [176].

The role of non-collagenous proteins in regulating the mineralisation process is of great interest in literature [177]. For example, non-collagenous proteins which are found at the borders of the collagen matrix attached to the minerals in the ECF inhibit crystal growth, while crystals that are not in contact with non-collagenous protein in the collagen matrix grow normally [175]. This study further concluded that the calcium movement into and out of hydroxyapatite is due to crystal growth and crystal dissolution, respectively.

Crystal growth and crystal dissolution occur through equilibrium processes at the surfaces and potentially explain the stability of the calcium supply demanded by all kinds of physiological processes [135, 136].

The role of the osteocyte, of which there are as many as tens of thousands per cubic millimetre of bone [49, 51, 53, 142], in the metabolism of phosphate has recently been investigated [178, 179]. Moreover, it is believed that osteocytes dissolve calcium from the peri-lacunar space and replace it according to demand, in order to maintain calcium homeostasis [176]. The process of calcium removal from the peri-lacunar matrix is called osteocytic osteolysis [180], which has been demonstrated recently in mice during lactation [138], confirming that osteocytes also actively participate in calcium homeostasis. Alterations in lacunar size have also been observed in response to changes in the mechanical environment, e.g. enlarged lacunae have been reported in mice after space flights [181] or after glucocorticoid

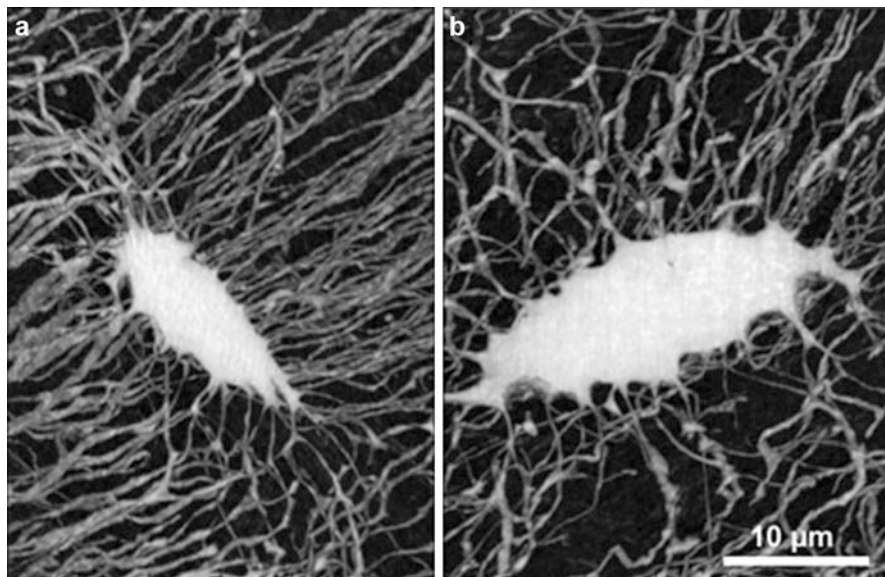


Fig. 1.8 Minimum intensity projections along z (a) and y (b) of one volume of interest containing the lacuna in the centre and the canaliculi pores connecting the lacunae to neighbouring cells. The size of the volume of interest is $z = 630$ pixel, $x = 800$ pixel and $y = 600$ pixel (200 pixel = 10 μm) [52]

treatment [182]. Both lacunar size and density were found to be altered in newly formed bone after anti-resorptive and anabolic pharmaceutical treatment in ovariectomised rats [183].

The distribution of osteocytes and their dendrites is thus not only crucial for proper sensing of mechanical signals across the bone matrix but also for easy access to mineral reservoirs. The distance between the extracellular tissue and the LCN is therefore of particular importance and has recently been demonstrated to be strongly related to the thickness and orientation of mineral particles and thus tissue quality [167]. The canalicular network provides a direct interface with the bone tissue which is much larger and much closer to the mineralised matrix compared to the interface formed by the lacunar walls [167] (Fig. 1.8). It has therefore been hypothesised that cell dendrites are involved in the active role of the osteocytes in tissue remodelling [138, 167, 184]. However, no measurement could support this hypothesis so far, possibly due to the lack of adequate three-dimensional quantitative imaging modalities at the length scales of the canaliculi [139].

In a recent study [52], we hypothesised that mineral exchange during mineralisation is achieved by the diffusion of minerals from the ECF in the LCN to the bone matrix, resulting in a gradual change in tissue mineralisation with respect to the distance from the pore-matrix interface. Based on this assumption, alterations in the mass density distribution with tissue age would be expected. In addition, we hypothesised that mineral exchange occurs not only at the lacunar but also at the canalicular boundaries.

We could provide evidence, by means of in-line phase nano-tomography, that the mass density in the direct vicinity of the LCN is indeed different from the mean mass density of the bone tissue, resulting in mass density gradients with respect to both the lacunar and the canalicular boundaries (Fig. 1.9).

The results indicated that mass density gradients diminished with increasing tissue age, resulting in a higher and a more homogeneously distributed extracellular matrix mass density in old tissue. These findings supported our hypothesis that extracellular matrix mineralisation is achieved through the diffusion of calcium from the extracellular fluid contained in the LCN to the bone matrix through all interfaces including the canaliculi. The smaller mass density values and gradients found in the peri-canalicular tissue compared to the peri-lacunar regions can be explained by the morphology of the LCN, indicating a higher mineral flux at the lacunar interfaces. We estimated that the amount of calcium stored in the subdomain of the bone tissue located within 0.5 μm distance from the LCN greatly exceeds the amount required for a rapidly exchangeable calcium pool to be used to compensate daily fluctuations in the serum calcium level. However, further studies are needed to confirm a mineral flux from the mineralised matrix into the LCN. Supporting the important role of this micropore network, we quantified the surface density (pore wall surface normalised to bone volume) of the LCN to be about 20 times higher than the surface density of the Haversian system. This relation holds despite the volume ratio of the lacunae being approximately one order of magnitude smaller than that of the Haversian canals.

In line with recent studies, these findings underlined the importance of the entire LCN in mineral homeostasis and the influence of its morphology on the spatial distribution of mass density in the mineralised extracellular matrix of bone. The role of the increased mass density adjacent to this pore network should therefore be taken into account in drug deposition studies and mechanical models studying the mechanosensation of osteocytes. Future studies using synchrotron radiation phase-contrast nano-computed tomography are expected to further aid the investigation of the diffusion and mineralisation processes and their coordination via osteocytes or other factors.

6 Conclusions and Future Perspective

6.1 Instrumentation

The work on in-line phase nano-CT shown here was performed on beamline ID22 at the ESRF. This beamline has now moved to the ID16 section and is run as a two-branch nano-imaging (ID16A) and nano-analysis (ID16B) beamline. The ID16A end station is located at 185 m from the source and is mainly dedicated to problems in biology, biomedicine and nanotechnology. It is optimised for high-resolution quantitative 3D imaging techniques with a specific focus on X-ray fluorescence and projection microscopy. This branch will be optimised for ultimate hard X-ray focusing of the beam (<20 nm) at specific energies (17 and 33.6 keV,

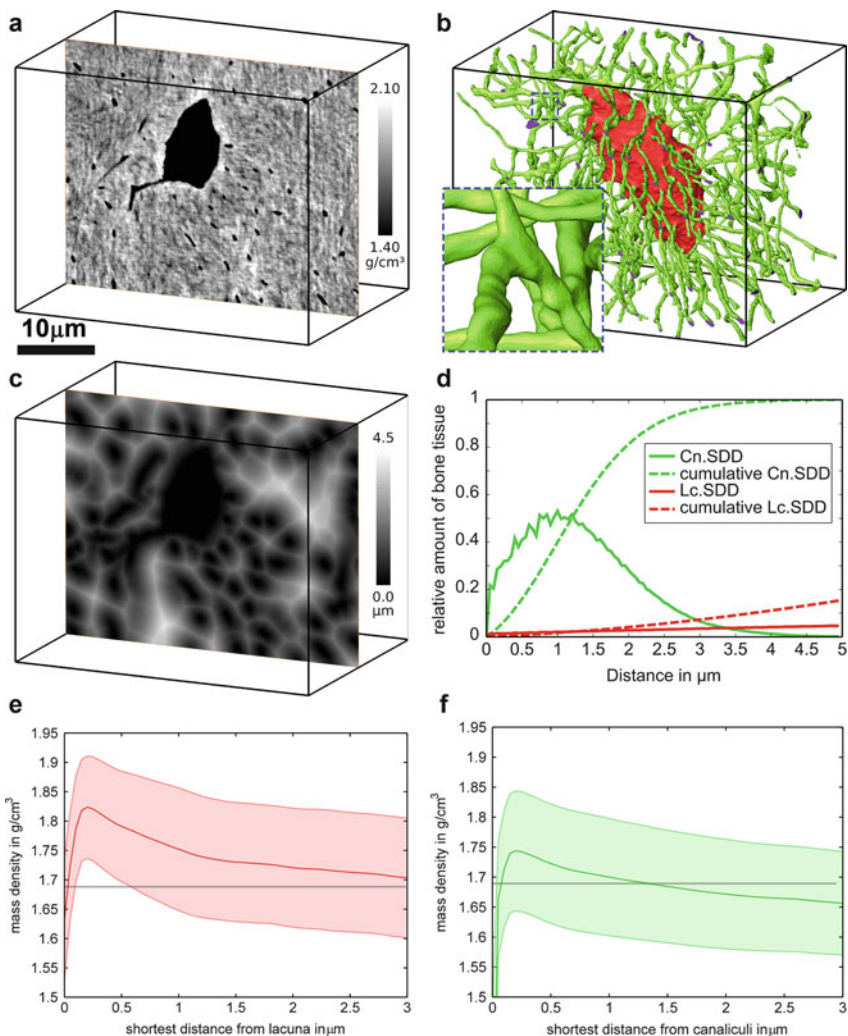


Fig. 1.9 Assessment of the peri-lacunar and peri-canalicular bone tissue mass densities based on in-line tomography images. (a) One slice of a volume of interest containing one osteocyte lacuna, cropped from the 3D reconstructed phase nano-CT image. The dimensions of the VOI are $800 \times 600 \times 630$ pixels. The greyscale corresponds to mass density. (b) Surface rendering of the lacunar (red) and canalicular (green) compartments segmented from the VOI. (c) Distance transform image showing the shortest distance from each point in the matrix to the lacunar-canalicular network. (d) Histogram of the 3D distance map (shortest distance distribution, SDD) of the canalicular (green) and the lacunar (red) boundaries shown together with their cumulative functions for the same VOI. From the solid lines, one can see that 50% of the bone tissue is situated within about 1.2 μm distance from the canalicular boundaries, while at this distance, the cumulative function of the histogram of the distances considering the lacuna is only about ten times smaller. (e and f) Average mass density and standard error bands as a function of the shortest distance to the osteocyte lacuna (e) and canaliculi (f), shown for the same VOI. The grey horizontal lines represent the mean mass density within the VOI [52]

$\Delta E/E \sim 10^{-2}$). The beamline uses fixed curvature multilayer coated KB optics. 3D nano-positioning is done using a metrologic reference under control of capacitive sensors and an on-line video microscope for sample placement. One main difference to the previous imaging implementation is that samples are imaged in a vacuum environment. In the future, cryo-cooling capabilities will be added to increase the scope for imaging in life science.

The ID16B end station, in parallel operation, is located at approximately 165 m from the source and is optimised for high-resolution (50 nm to 1 μm) spectroscopic applications ($\Delta E/E \sim 10^{-4}$), including X-ray fluorescence (XRF), X-ray absorption spectroscopy (XAS) and X-ray-excited optical luminescence. It offers a multimodal approach (XAS, XRD, XRI) capable of in situ experiments. In a complementary way to the ID16A end station, ID16B will provide a monochromatic beam tuneable over a large energy range (5–70 keV). The ID16 beamlines opened for user experiments in late 2014.

6.2 Bone Nano-imaging

The above described technological advancements are expected to provide further insights into the structure and function of bone on the submicron scale. An important issue to be addressed here is the detailed morphology of canaliculi and in particular the interface of the osteocyte dendrites and the mineralised extracellular tissue. Moreover, the geometries of both the osteocytes and its pericellular space filled with interstitial fluid are of high interest. These details should provide the basis for image analysis and finite element methods aiming at unravelling the not yet fully understood mechanosensation of these cells. The interaction of osteocytes with the mineralised matrix, in the context of both remodelling and mineral homeostasis, could be more efficiently analysed with even higher-resolution imaging. Bone tissue structure, density and composition at the direct vicinity of the cells are of highest interest in this respect. Even more accurate and detailed data on collagen orientation also around the LCN porosity would allow for better description of the mechanical properties of bone at these fine scales. Besides the topic of microcrack formation, more exact description of the deformations arriving to the cell through the heterogeneous and anisotropic bone tissue could be better analysed in possession of the higher-resolution image data.

Due to the high sensitivity of in-line phase tomography, it should also be possible to image the osteocytes directly in situ. We have some indication that there is enough contrast to do this (Fig. 1.10). Note that the cells seem severely shrunken, in a similar manner to what has earlier been observed with electron microscopy [185]. Also note that these structures are different from the mineralised ones reported in Ref. [142]; the structures shown here are very weakly contrasted, as opposed to those in Ref. [142]. No particular care was taken in the sample preparation with respect to cell preservation, however. Again, as in electron microscopy, the most important aspect for the in situ 3D observation of the osteocyte is probably the sample preparation [169]. Several options can be investigated; the future cryo-tomography capabilities

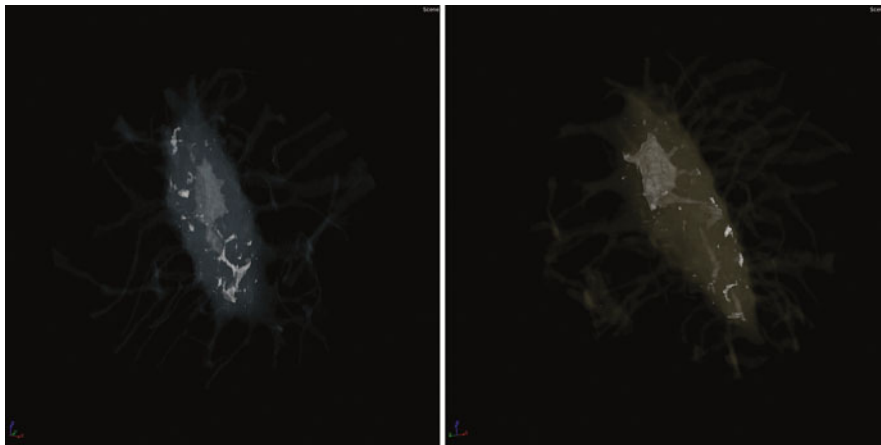


Fig. 1.10 Renderings of soft tissue preservations inside osteocyte lacunae, imaged in situ in dry bone using in-line phase nano-CT. The bone matrix is rendered as transparent, the lacuna and canaliculi are rendered in semi-transparent colour and the soft tissue preservations are rendered in *white*. Note the severely shrunken aspect of the eventual osteocytes. This indicates that contrast is probably sufficient for in situ osteocyte imaging, but that special care needs to be taken with respect to the sample preparation. The size of the box showing the renderings is approximately $40\ \mu\text{m} \times 40\ \mu\text{m}$

of ID16A will be used to this effect, for example. Preservation of cell geometry is known to require special sample preparation techniques, which will be a challenging part of future nano-CT experiments in this direction. The applicability of previously established methods towards this end has to be explored, and there may be a need for the development of new approaches.

Acknowledgements We would like to thank Françoise Peyrin, Peter Cloetens, Kay Raum and Alexandra Pacureanu for their contributions to the work presented here.

This work was supported by the LABEX PRIMES (ANR-11-LABX-0063) of Université de Lyon, within the programme “Investissements d’Avenir” (ANR-11-IDEX-0007) operated by the French National Research Agency (ANR).

References

1. Röntgen WC (1896) On a new kind of rays. *Nature* 53:274–277
2. Cormack AM (1963) Representation of a function by its line integrals, with some radiological applications. *J Appl Phys* 34:2722
3. Hounsfield GN (1972) A method and apparatus for examination of a body by radiation such as X-ray or gamma radiation. 1283915
4. Bonse U (2002) Developments in X-ray tomography II. In: *Proceedings of the SPIE*, vol. 4503
5. Bouxsein ML, Boyd SK, Christiansen BA, Guldberg RE, Jepsen KJ, Müller R (2010) Guidelines for assessment of bone microstructure in rodents using micro-computed tomography. *J Bone Miner Res* 25(7):1468–1486
6. Engelke K, Karolczak M, Lutz A, Seibert U, Schaller S, Kalender W (1999) Micro-CT. Technology and application for assessing bone structure. *Radiologie* 39(3):203–212

7. Hildebrand T, Laib A, Müller R, Dequeker J, Rügsegger P (1999) Direct three-dimensional morphometric analysis of human cancellous bone: microstructural data from spine, femur, iliac crest, and calcaneus. *J Bone Miner Res* 14(7):1167–1174
8. Salomé M, Peyrin F, Cloetens P, Odet C, Laval-Jeantet A-M, Baruchel J, Spanne P (1999) A synchrotron radiation microtomography system for the analysis of trabecular bone samples. *Med Phys* 26(10):2194
9. Nuzzo S, Peyrin FF, Cloetens P, Baruchel JJ, Boivin G (2002) Quantification of the degree of mineralization of bone in three dimensions using synchrotron radiation microtomography. *Med Phys* 29(11):2672
10. Peyrin F, Salomé M, Nuzzo S, Cloetens P, Laval-Jeantet AM, Baruchel J (2000) Perspectives in three-dimensional analysis of bone samples using synchrotron radiation microtomography. *Cell Mol Biol* 46(6):1089–1102
11. Schneider P, Meier M, Wepf R, Müller R (2010) Towards quantitative 3D imaging of the osteocyte lacuno-canalicular network. *Bone* 47(5):848–858
12. van Hove RP, Nolte PA, Vatsa A, Semeins CM, Salmon PL, Smit TH, Klein-Nulend J (2009) Osteocyte morphology in human tibiae of different bone pathologies with different bone mineral density – is there a role for mechanosensing? *Bone* 45(2):321–329
13. Labiche J-C, Mathon O, Pascarelli S, Newton MA, Ferre GG, Curfs C, Vaughan G, Homs A, Carreiras DF (2007) Invited article: the fast readout low noise camera as a versatile x-ray detector for time resolved dispersive extended x-ray absorption fine structure and diffraction studies of dynamic problems in materials science, chemistry, and catalysis. *Rev Sci Instrum* 78(9):091301
14. Paschalis EP, Mendelsohn R, Boskey AL (2011) Infrared assessment of bone quality: a review. *Clin Orthop Relat Res* 469(8):2170–2178
15. Seeman E, Delmas PD (2006) Bone quality – the material and structural basis of bone strength and fragility. *N Engl J Med* 354(21):2250–2261
16. Bonewald LF (2006) Mechanosensation and transduction in osteocytes. *Bonekey Osteovision* 3(10):7–15
17. Klein-Nulend J, Bacabac RG, Mullender MG (2005) Mechanobiology of bone tissue. *Pathol Biol* 53(10):576–580
18. Knothe Tate ML, Adamson JR, Tami AE, Bauer TW, Nijweide PJ, Burger EH, Nulend JK (2004) The osteocyte. *Int J Biochem Cell Biol* 36(1):1–8
19. Nijweide PJ, Burger EH, Nulend JK (2002) The osteocyte, pp 93–108
20. Burger EH, Klein-Nulend J (1999) Mechanotransduction in bone – role of the lacuno-canalicular network. *FASEB J* 13(Suppl):S101–S112
21. Nicoletta D, Feng J (2008) Effects of nanomechanical bone tissue properties on bone tissue strain: implications for osteocyte mechanotransduction. *J Musculoskelet* 8(4):330–331
22. Verbruggen SW, Vaughan TJ, McNamara LM (2012) Strain amplification in bone mechanobiology: a computational investigation of the in vivo mechanics of osteocytes. *J R Soc Interface* 9(75):2735–2744
23. Verbruggen SW, Vaughan TJ, McNamara LM (2013) Fluid flow in the osteocyte mechanical environment: a fluid–structure interaction approach. *Biomech Model Mechanobiol*, epub, Apr 2013
24. Hazenberg JG, Freeley M, Foran E, Lee TC, Taylor D (2006) Microdamage: a cell transducing mechanism based on ruptured osteocyte processes. *J Biomech* 39(11):2096–2103
25. Taylor D, Hazenberg JG, Lee TC (2007) Living with cracks: damage and repair in human bone. *Nat Mater* 6(4):263–268
26. Qiu S, Rao DS, Fyhrie DP, Palnitkar S, Parfitt AM (2005) The morphological association between microcracks and osteocyte lacunae in human cortical bone. *Bone* 37(1):10–15
27. Dooley C, Tisbo P, Lee TC, Taylor D (2012) Rupture of osteocyte processes across microcracks: the effect of crack length and stress. *Biomech Model Mechanobiol* 11(6):759–766

28. Bonewald LF, Kneissel M, Johnson M (2013) Preface: the osteocyte. *Bone* 54(2):181
29. Bonewald LF (2011) The amazing osteocyte. *J Bone Miner Res* 26(2):229–238
30. Kalajzic I, Matthews BG, Torreggiani E, Harris MA, Divieti Pajevic P, Harris SE (2013) In vitro and in vivo approaches to study osteocyte biology. *Bone* 54(2):296–306
31. Klein-Nulend J, Bakker AD, Bacabac RG, Vatsa A, Weinbaum S (2013) Mechanosensation and transduction in osteocytes. *Bone* 54(2):182 (in press)
32. Rochefort GY, Pallu S, Benhamou CL (2010) Osteocyte : the unrecognized side of bone tissue. *Osteoporos Int* 21(9):1457–1469
33. Seeman E (2006) Osteocytes – martyrs for integrity of bone strength. *Osteoporos Int* 17(10):1443–1448
34. Atkins A, Dean MN, Habegger ML, Motta PJ, Ofer L, Repp F, Shipov A, Weiner S, Currey JD, Shahar R (2014) Remodeling in bone without osteocytes: billfish challenge bone structure-function paradigms. *Proc Natl Acad Sci U S A* 111(45):16047–16052
35. Burr DB, Schaffler MB, Frederickson RG (1988) Composition of the cement line and its possible mechanical role as a local interface in human compact bone. *J Biomech* 21(11):939–945
36. Schaffler MB, Burr DB, Frederickson RG (1987) Morphology of the osteonal cement line in human bone. *Anat Rec* 217(3):223–228
37. Davies JE (2007) Bone bonding at natural and biomaterial surfaces. *Biomaterials* 28(34):5058–5067
38. Skedros JG, Holmes JL, Vajda EG, Bloebaum RD (2005) Cement lines of secondary osteons in human bone are not mineral-deficient: new data in a historical perspective. *Anat Rec A: Discov Mol Cell Evol Biol* 286(1):781–803
39. Milovanovic P, Zimmermann EAE, Hahn M, Djonic D, Püschel K, Djuric M, Amling M, Busse B (2013) Osteocytic canalicular networks: morphological implications for altered mechanosensitivity. *ACS* 7(9):7542–7551
40. Kingsmill VJ, Boyde A (1998) Mineralisation density of human mandibular bone: quantitative backscattered electron image analysis. *J Anat* 192(Pt 2):245–256
41. Pannarale L, Braidotti P, d'Alba L, Gaudio E (1994) Scanning electron microscopy of collagen fiber orientation in the bone lamellar system in non-decalcified human samples. *Acta Anat (Basel)* 151(1):36–42
42. Reznikov N, Almany-Magal R, Shahar R, Weiner S (2013) Three-dimensional imaging of collagen fibril organization in rat circumferential lamellar bone using a dual beam electron microscope reveals ordered and disordered. *Bone* 52(2):676–683
43. Reznikov N, Shahar R, Weiner S (2014) Three-dimensional structure of human lamellar bone: the presence of two different materials and new insights into the hierarchical organization. *Bone* 59(2012):93–104
44. Giraud-Guille M-M, Besseau L, Martin R (2003) Liquid crystalline assemblies of collagen in bone and in vitro systems. *J Biomech* 36(10):1571–1579
45. Hassenkam T, Fantner GE, Cutroni JA, Weaver JC, Morse DE, Hansma PK (2004) High-resolution AFM imaging of intact and fractured trabecular bone. *Bone* 35(1):4–10
46. Bromage TG, Goldman HM, McFarlin SC, Warshaw J, Boyde A, Riggs CM (2003) Circularly polarized light standards for investigations of collagen fiber orientation in bone. *Anat Rec B New Anat* 274(1):157–168
47. Kazanci M, Roschger P, Paschalis EP, Klaushofer K, Fratzl P (2006) Bone osteonal tissues by Raman spectral mapping: orientation-composition. *J Struct Biol* 156(3):489–496
48. Schrof S, Varga P, Galvis L, Raum K, Masic A (2014) 3D Raman mapping of the collagen fibril orientation in human osteonal lamellae. *J Struct Biol* 187(3):266–275
49. Carter Y, Thomas CDL, Clement JG, Peele AG, Hannah K, Cooper DMLL (2013) Variation in osteocyte lacunar morphology and density in the human femur – a synchrotron radiation micro-CT study. *Bone* 52(1):126–132
50. Carter Y, Thomas CDL, Clement JG, Cooper DML (2013) Femoral osteocyte lacunar density, volume and morphology in women across the lifespan. *J Struct Biol* 183(3):519–526

51. Dong P, Hauptert S, Hesse B, Langer M, Gouttenoire P-J, Bousson V, Peyrin F (2014) 3D osteocyte lacunar morphometric properties and distributions in human femoral cortical bone using synchrotron radiation micro-CT images. *Bone* 60:172–185
52. Hesse B, Varga P, Langer M, Pacureanu A, Schrof S, Männicke N, Suhonen H, Maurer P, Cloetens P, Peyrin F, Raum K (2014) Canalicular network morphology is the major determinant of the spatial distribution of mass density in human bone tissue – evidence by means of synchrotron radiation phase-contrast nano-CT. *J Bone Miner Res* 30(2):346–356
53. Hesse B, Langer M, Varga P, Pacureanu A, Dong P, Schrof S, Männicke N, Suhonen H, Olivier C, Maurer P, Kazakia GJ, Raum K, Peyrin F (2014) Alterations of mass density and 3D osteocyte lacunar properties in bisphosphonate-related osteonecrotic human jaw Bone, a synchrotron μ CT study. *PLoS One* 9(2), e88481
54. Pacureanu A, Langer M, Boller E, Tafforeau P, Peyrin FF (2012) Nanoscale imaging of the bone cell network with synchrotron x-ray tomography: optimization of acquisition setup. *Med Phys* 39(4):2229–2238
55. Pacureanu A, Larrue A, Langer M, Olivier C, Muller C, Lafage-Proust M-H, Peyrin F (2013) Adaptive filtering for enhancement of the osteocyte cell network in 3D microtomography images. *IRBM* 34(1):48–52
56. Sugawara Y, Kamioka H, Honjo T, Tezuka K, Takano-Yamamoto T (2005) Three-dimensional reconstruction of chick calvarial osteocytes and their cell processes using confocal microscopy. *Bone* 36(5):877–883
57. Gourion-Arsiquaud S, Marcott C, Hu Q, Boskey AL (2014) Studying variations in bone composition at nano-scale resolution: a preliminary report. *Calcif Tissue Int* 95(5):413–418
58. Geith T, Amarie S, Milz S, Bamberg F, Keilmann F (2014) Visualisation of methacrylate-embedded human bone sections by infrared nanoscopy. *J Biophotonics* 7(6):418–424
59. Schneider P, Meier M, Wepf R, Müller R (2011) Serial FIB/SEM imaging for quantitative 3D assessment of the osteocyte lacuno-canalicular network. *Bone* 49(2):304–311
60. Magal RA, Reznikov N (2014) Three-dimensional structure of minipig fibrolamellar bone: adaptation to axial loading. *J Struct* 186(2):253–264
61. Kamioka H, Murshid SA, Ishihara Y, Kajimura N, Hasegawa T, Ando R, Sugawara Y, Yamashiro T, Takaoka A, Takano-Yamamoto T (2009) A method for observing silver-stained osteocytes in situ in 3-microm sections using ultra-high voltage electron microscopy tomography. *Microsc Microanal* 15(5):377–383
62. Martínez-Criado G, Tucoulou R, Cloetens P, Bleuët P, Bohic S, Cauzid J, Kieffer I, Kosior E, Labouré S, Petitgirard S, Rack A, Sans JA, Segura-Ruiz J, Suhonen H, Susini J, Villanova J (2012) Status of the hard x-ray microprobe beamline ID22 of the European Synchrotron Radiation Facility. *J Synchrotron Radiat* 19(Pt 1):10–18
63. Morawe C, Hignette O, Cloetens P, Ludwig W, Borel C, Bernard P, Rommeveaux A (2006) Graded multilayers for focusing hard x-rays below 50 nm. In: *SPIE optics + photonics*, pp 63170F–63170F-11
64. Barrett R, Baker R, Cloetens P, Dabin Y, Morawe C, Suhonen H, Tucoulou R, Vivo A, Zhang L (2011) Dynamically-figured mirror system for high-energy nanofocusing at the ESRF. In: *SPIE optical engineering + applications*. pp 813904–813904-12
65. Hignette O, Cloetens P, Morawe C, Borel C, Ludwig W, Bernard P, Rommeveaux A, Bohic S (2007) Nanofocusing at ESRF using graded multilayer mirrors. *AIP Conf Proc* 879(1):792–795
66. Zhang L, Baker R, Barrett R, Cloetens P, Dabin Y, Garrett R, Gentle I, Nugent K, Wilkins S (2010) Mirror profile optimization for nano-focusing KB mirror. In: *SRI 2009, 10th international conference on radiation instrumentation*, vol 1234(1), pp 801–804
67. Cloetens P, Suhonen H, Bay A, Bohic S, Fleck C, Langer M, Pacureanu A, Peyrin F, Rack A, Vigneron JP, Zaslansky P (2012) Non-destructive and multi-modal 3D imaging of biological materials. In: *2012 MRS spring meeting and exhibit*
68. Tucoulou R, Martínez-Criado G, Bleuët P, Kieffer I, Cloetens P, Labouré S, Martin T, Guilloud C, Susini J (2008) High-resolution angular beam stability monitoring at a nanofocusing beamline. *J Synchrotron Radiat* 15(Pt 4):392–398

69. Jackson JD (1975) Classical electrodynamics
70. Snigirev A, Snigireva I, Kohn V, Kuznetsov S, Schelokov I (1995) On the possibilities of x-ray phase contrast microimaging by coherent high-energy synchrotron radiation. *Rev Sci Instrum* 66(12):5486
71. Goodman JW (2005) Introduction to fourier optics
72. Langer M, Pacureanu A, Suhonen H, Grimal Q, Cloetens P, Peyrin F (2012) X-ray phase nanotomography resolves the 3D human bone ultrastructure. *PLoS One* 7(8), e35691
73. Cloetens P, Ludwig W, Baruchel J, Van Dyck D, Van Landuyt J, Guigay JP, Schlenker M (1999) Holotomography: quantitative phase tomography with micrometer resolution using hard synchrotron radiation x rays. *Appl Phys Lett* 75(19):2912
74. Langer M, Cloetens P, Guigay J-P, Peyrin F (2008) Quantitative comparison of direct phase retrieval algorithms in in-line phase tomography. *Med Phys* 35(10):4556–4566
75. Elser V (2003) Solution of the crystallographic phase problem by iterated projections. *Acta Crystallogr Sect A: Found Crystallogr* 59(3):201–209
76. Fienup JR (1982) Phase retrieval algorithms: a comparison. *Appl Opt* 21(15):2758–2769
77. Gerchberg RW, Saxton WO (1972) A practical algorithm for the determination of phase from image and diffraction plane pictures. *Optik (Stuttg)* 35:237–246
78. Bauschke HH, Combettes PL, Luke DR (2002) Phase retrieval, error reduction algorithm, and Fienup variants: a view from convex optimization. *J Opt Soc Am A* 19(7):1334
79. Thibault P, Elser V (2010) X-ray diffraction microscopy. *Annu Rev Condens Matter Phys* 1(1):237–255
80. Elser V, Rankenburg I, Thibault P (2007) Searching with iterated maps. *Proc Natl Acad Sci U S A* 104(2):418–423
81. Dierolf M, Menzel A, Thibault P, Schneider P, Kewish CM, Wepf R, Bunk O, Pfeiffer F (2010) Ptychographic x-ray computed tomography at the nanoscale. *Nature* 467(7314):436–439
82. Schroer C, Boye P, Feldkamp J, Patommel J, Schropp A, Schwab A, Stephan S, Burghammer M, Schöder S, Riekel C (2008) Coherent X-ray diffraction imaging with nanofocused illumination. *Phys Rev Lett* 101(9):090801
83. Huang X, Nelson J, Kirz J, Lima E, Marchesini S, Miao H, Neiman A, Shapiro D, Steinbrener J, Stewart A, Turner J, Jacobsen C (2009) Soft X-ray diffraction microscopy of a frozen hydrated yeast cell. *Phys Rev Lett* 103(19):198101
84. Maiden AM, Rodenburg JM (2009) An improved ptychographical phase retrieval algorithm for diffractive imaging. *Ultramicroscopy* 109(10):1256–1262
85. Thibault P, Dierolf M, Menzel A, Bunk O, David C, Pfeiffer F (2008) High-resolution scanning x-ray diffraction microscopy. *Science* 321(5887):379–382
86. Thibault P, Dierolf M, Bunk O, Menzel A, Pfeiffer F (2009) Probe retrieval in ptychographic coherent diffractive imaging. *Ultramicroscopy* 109(4):338–343
87. Hoppe W (1969) Beugung im inhomogenen Primärstrahlwellenfeld. I. Prinzip einer Phasenmessung von Elektronenbeugungsinterferenzen. *Acta Crystallogr Sect A* 25(4):495–501
88. Guinier A (1994) X-ray diffraction in crystals, imperfect crystals, and amorphous bodies. Courier Dover Publications
89. Langer M, Cloetens P, Peyrin F (2010) Regularization of phase retrieval with phase-attenuation duality prior for 3-D holotomography. *IEEE Trans Image Process* 19(9):2428–2436
90. Paganin D, Mayo SC, Gureyev TE, Miller PR, Wilkins SW (2002) Simultaneous phase and amplitude extraction from a single defocused image of a homogeneous object. *J Microsc* 206(1):33–40
91. Wilkins SW, Gureyev TE, Gao D, Pogany A, Stevenson AW (1996) Phase-contrast imaging using polychromatic hard x-rays. *Nature* 384(6607):335–338
92. Holler M, Diaz A, Guizar-Sicairos M, Karvinen P, Färm E, Härkönen E, Ritala M, Menzel A, Raabe J, Bunk O (2014) X-ray ptychographic computed tomography at 16 nm isotropic 3D resolution. *Sci Rep* 4:3857

93. Dennis MDP, Ghiglia C (1998) Two-dimensional phase unwrapping: theory, algorithms, and software. Wiley, New York
94. Andrews JC, Almeida E, van der Meulen MCH, Alwood JS, Lee C, Liu Y, Chen J, Meirer F, Feser M, Gelb J, Rudati J, Tkachuk A, Yun W, Pianetta P (2010) Nanoscale x-ray microscopic imaging of mammalian mineralized tissue. *Microsc Microanal* 16(3):327–336
95. Mokso R, Cloetens P, Maire E, Ludwig W, Buffière J-Y (2007) Nanoscale zoom tomography with hard x rays using Kirkpatrick-Baez optics. *Appl Phys Lett* 90(14):144104
96. Guigay JP, Langer M, Boistel R, Cloetens P (2007) Mixed contrast transfer and transport of intensity approach for phase retrieval in the Fresnel region. *Opt Lett* 32:1617–1619
97. Langer M, Hesse B, Pacureanu A, Suhonen H, Cloetens P, Raum K, Peyrin F (2013) Priors for x-ray in-line phase tomography of heterogeneous objects. *Phil Trans R Soc A* 372: 20130129
98. Langer M, Cloetens P, Hesse B, Pacureanu A, Raum K, Lafage-Proust M-H, Peyrin F (2012) X-ray in-line phase micro-CT for simultaneous bone and soft tissue visualisation. In: *Nouvelles méthodologies en imagerie du vivant*, p 9581
99. Langer M, Cloetens P, Peyrin F (2009) Fourier-wavelet regularization of phase retrieval in x-ray in-line phase tomography. *J Opt Soc Am A Opt Image Sci Vis* 26(8):1876–1881
100. Davidoiu V, Sixou B, Langer M, Peyrin F (2011) Non-linear iterative phase retrieval based on Fréchet derivative and projection operators. *Opt Express* 19(23):106–109
101. Davidoiu V, Sixou B, Langer M, Peyrin F (2013) Nonlinear approaches for the single-distance phase retrieval problem involving regularizations with sparsity constraints. *Appl Opt* 52(17):3977–3986
102. Davidoiu V, Sixou B, Langer M, Peyrin F (2013) In-line phase tomography using nonlinear phase retrieval. *Ann Univ Bucharest Math Ser* 4(LXII):115–122
103. Moosmann J, Hofmann R, Baumbach T (2011) Single-distance phase retrieval at large phase shifts. *Opt Express* 19:12066–12073
104. Moosmann J, Hofmann R, Bronnikov A, Baumbach T (2010) Nonlinear phase retrieval from single-distance radiograph. *Opt Express* 18:25771–25785
105. Gebhardt W (1906) Ueber funktionell wichtige Anordnungsweisen der groberen und feineren Bauelemente des Wirbeltierknochens. *Arch Entw Mech* 20:187–322
106. Wang Y, Azaïs T, Robin M, Vallée A, Catania C, Legriel P, Pehau-Arnaudet G, Babonneau F, Giraud-Guille M-M, Nassif N (2012) The predominant role of collagen in the nucleation, growth, structure and orientation of bone apatite. *Nat Mater* 11(8):724–733
107. Fratzl P, Weinkamer R (2007) Nature's hierarchical materials. *Prog Mater Sci* 52(8):1263–1334
108. Ascenzi A, Bonucci E (1967) The tensile properties of single osteons. *Anat Rec* 158(4):375–386
109. Ascenzi A, Bonucci E (1968) The compressive properties of single osteons. *Anat Rec* 161(3):377–391
110. Ascenzi A, Bonucci E (1972) The shearing properties of single osteons. *Anat Rec* 172(3):499–510
111. Ascenzi A, Benvenuti A, Bonucci E (1982) The tensile properties of single osteonic lamellae: technical problems and preliminary results. *J Biomech* 15(1):29–37
112. Giraud-Guille MM (1988) Twisted plywood architecture of collagen fibrils in human compact bone osteons. *Calcif Tissue Int* 42(3):167–180
113. Marotti G, Muglia MA, Palumbo C (1994) Structure and function of lamellar bone. *Clin Rheumatol* 13(Suppl 1):63–68
114. Weiner S, Arad T, Sabanay I, Traub W (1997) Rotated plywood structure of primary lamellar bone in the rat: orientations of the collagen fibril arrays. *Bone* 20(6):509–514
115. Ascenzi MG, Ascenzi A, Benvenuti A, Burghammer M, Panzavolta S, Bigi A (2003) Structural differences between 'dark' and 'bright' isolated human osteonic lamellae. *J Struct Biol* 141(1):22–33

116. Ascenzi M-G, Lomovtsev A (2006) Collagen orientation patterns in human secondary osteons, quantified in the radial direction by confocal microscopy. *J Struct Biol* 153(1):14–30
117. Hofmann T, Heyroth F, Meinhard H, Fränzel W, Raum K (2006) Assessment of composition and anisotropic elastic properties of secondary osteon lamellae. *J Biomech* 39(12): 2282–2294
118. Kazanci M, Wagner HD, Manjubala NI, Gupta HS, Paschalis E, Roschger P, Fratzl P (2007) Raman imaging of two orthogonal planes within cortical bone. *Bone* 41(3):456–461
119. Spiesz EM, Kaminsky W, Zysset PK (2011) A quantitative collagen fibers orientation assessment using birefringence measurements: calibration and application to human osteons. *J Struct Biol* 176(3):302–306
120. Gourrier A, Wagermaier W, Burghammer M, Lammie D, Gupta HS, Fratzl P, Riekel C, Wess TJ, Paris O (2007) Scanning x-ray imaging with small-angle scattering contrast. *J Appl Crystallogr* 40(s1):s78–s82
121. Seidel R, Gourrier A, Kerschitzki M, Burghammer M, Fratzl P, Gupta HS, Wagermaier W (2011) Synchrotron 3D SAXS analysis of bone nanostructure. *Bioinspired Biomim Nanobiomaterials* 1:123–131
122. Granke M, Gourrier A, Rupin F, Raum K, Peyrin F, Burghammer M, Saïed A, Laugier P (2013) Microfibril orientation dominates the microelastic properties of human bone tissue at the lamellar length scale. *PLoS One* 8(3), e58043
123. Wagermaier W, Gupta HS, Gourrier A, Paris O, Roschger P, Burghammer M, Riekel C, Fratzl P (2007) Scanning texture analysis of lamellar bone using microbeam synchrotron x-ray radiation. *J Appl Crystallogr* 40(1):115–120
124. Wagermaier W, Gupta HS, Gourrier A, Burghammer M, Roschger P, Fratzl P (2006) Spiral twisting of fiber orientation inside bone lamellae. *Biointerphases* 1(1):1
125. Marotti G (1993) A new theory of bone lamellation. *Calcif Tissue Int* 53(Suppl 1):S47–S55; discussion S56
126. Marotti G, Ferretti M, Palumbo C (2013) The problem of bone lamellation: an attempt to explain different proposed models. *J Morphol* 274(5):543–550
127. Varga P, Pacureanu A, Langer M, Suhonen H, Hesse B, Grimal Q, Cloetens P, Raum K, Peyrin F (2013) Investigation of the 3D orientation of mineralized collagen fibrils in human lamellar bone using synchrotron x-ray phase nano-tomography. *Acta Biomater* 9:8118–8127
128. Rho JY, Kuhn-Spearing L, Zioupos P (1998) Mechanical properties and the hierarchical structure of bone. *Med Eng Phys* 20(2):92–102
129. Ritchie RO (2011) The conflicts between strength and toughness. *Nat Mater* 10(11):817–822
130. Marotti G (1993) Calcified tissue a new theory of bone lamellation, vol 53
131. Gupta HS, Stachewicz U, Wagermaier W, Roschger P, Wagner HD, Fratzl P (2006) Mechanical modulation at the lamellar level in osteonal bone. *J Mater Res* 21:1913–1921
132. Reisinger AG, Pahr DH, Zysset PK (2011) Elastic anisotropy of bone lamellae as a function of fibril orientation pattern. *Biomech Model Mechanobiol* 10(1):67–77
133. Camelli D, Vena P, Dao M, Ortiz C, Contro R (2013) Orientation and size-dependent mechanical modulation within individual secondary osteons in cortical bone tissue. *J R Soc Interface* 10(81):20120953
134. Faingold A, Cohen SR, Reznikov N, Wagner HD (2013) Osteonal lamellae elementary units: lamellar microstructure, curvature and mechanical properties. *Acta Biomater* 9(4):5956–5962
135. Chen X, Nadiarynh O, Plotnikov S, Campagnola PJ (2012) Second harmonic generation microscopy for quantitative analysis of collagen fibrillar structure. *Nat Protoc* 7(4):654–669
136. Williams RM, Zipfel WR, Webb WW (2005) Interpreting second-harmonic generation images of collagen I fibrils. *Biophys J* 88(2):1377–1386
137. Currey JD, Shahar R (2013) Cavities in the compact bone in tetrapods and fish and their effect on mechanical properties. *J Struct Biol* 183(2):107–122
138. Qing H, Ardeshirpour L, Pajevic PD, Dusevich V, Jähn K, Kato S, Wysolmerski J, Bonewald LF (2012) Demonstration of osteocytic perilacunar/canalicular remodeling in mice during lactation. *J Bone Miner Res* 27(5):1018–1029

139. Webster DJ, Schneider P, Dallas SL, Müller R (2013) Studying osteocytes within their environment. *Bone* (in press)
140. Vatsa A, Breuls RG, Semeins CM, Salmon PL, Smit TH, Klein-Nulend J (2008) Osteocyte morphology in fibula and calvaria – is there a role for mechanosensing? *Bone* 43(3):452–458
141. Hannah KM, Thomas CDL, Clement JG, De Carlo F, Peele AG (2010) Bimodal distribution of osteocyte lacunar size in the human femoral cortex as revealed by micro-CT. *Bone* 47(5):866–871
142. Hesse B, Männicke N, Pacureanu A, Varga P, Langer M, Maurer P, Peyrin F, Raum K (2014) Accessing osteocyte lacunar geometrical properties in human jaw bone on the submicron length scale using synchrotron radiation μ CT. *J Microsc* 255(3):158–168
143. Dong P, Pacureanu A, Zuluaga MA, Olivier C, Grimal Q, Peyrin F (2014) Quantification of the 3D morphology of the bone cell network from synchrotron micro-ct images. *Image Anal Stereol* 33(2):157
144. Mullender MG, Tan SD, Vico L, Alexandre C, Klein-Nulend J (2005) Differences in osteocyte density and bone histomorphometry between men and women and between healthy and osteoporotic subjects. *Calcif Tissue Int* 77(5):291–296
145. Knothe Tate ML, Tami A, Bauer TW, Knothe U (2002) Micropathoanatomy of osteoporosis – indications for a cellular basis of bone disease. *Adv Osteoporotic Fract Manag* 2(1):9–14
146. Loisel AE, Jiang JX, Donahue HJ (2013) Gap junction and hemichannel functions in osteocytes. *Bone* 54(2):205–212
147. Price C, Zhou X, Li W, Wang L (2011) Real-time measurement of solute transport within the lacunar-canalicular system of mechanically loaded bone: direct evidence for load-induced fluid flow. *J Bone Miner Res* 26(2):277–285
148. You L-D, Weinbaum S, Cowin SC, Schaffler MB (2004) Ultrastructure of the osteocyte process and its pericellular matrix. *Anat Rec A: Discov Mol Cell Evol Biol* 278(2):505–513
149. Wang Y, McNamara LM, Schaffler MB, Weinbaum S (2007) A model for the role of integrins in flow induced mechanotransduction in osteocytes. *Proc Natl Acad Sci U S A* 104(40):15941–15946
150. Nguyen AM, Jacobs CR (2013) Emerging role of primary cilia as mechanosensors in osteocytes. *Bone* 54(2):196–204
151. Stern AR, Nicolella DP (2013) Measurement and estimation of osteocyte mechanical strain. *Bone* 54(2):191–195
152. Group M, Hero S, Burr DB (1996) In vivo measurement of human tibial strains during vigorous activity 18(5)
153. You L, Cowin SC, Schaffler MB, Weinbaum S (2001) A model for strain amplification in the actin cytoskeleton of osteocytes due to fluid drag on pericellular matrix. *J Biomech* 34(11):1375–1386
154. Nicolella DP, Moravits DE, Gale AM, Bonewald LF, Lankford J (2006) Osteocyte lacunae tissue strain in cortical bone. *J Biomech* 39(9):1735–1743
155. Weinbaum S, Cowin SC, Zeng Y (1994) A model for the excitation of osteocytes by mechanical loading-induced bone fluid shear stresses. *J Biomech* 27(3):339–360
156. Han Y, Cowin SC, Schaffler MB, Weinbaum S (2004) Mechanotransduction and strain amplification in osteocyte cell processes. *Proc Natl Acad Sci U S A* 101(47):16689–16694
157. McCreddie BR, Hollister SJ, Schaffler MB, Goldstein SA (2004) Osteocyte lacuna size and shape in women with and without osteoporotic fracture. *J Biomech* 37(4):563–572
158. Bonivitch AR, Bonewald LF, Nicolella DP (2007) Tissue strain amplification at the osteocyte lacuna: a microstructural finite element analysis. *J Biomech* 40(10):2199–2206
159. Deligianni DD, Apostolopoulos CA (2008) Multilevel finite element modeling for the prediction of local cellular deformation in bone. *Biomech Model Mechanobiol* 7(2):151–159

160. Anderson EJ, Knothe Tate ML (2008) Idealization of pericellular fluid space geometry and dimension results in a profound underprediction of nano-microscale stresses imparted by fluid drag on osteocytes. *J Biomech* 41(8):1736–1746
161. Rath AL, Bonewald LF, Ling J, Jiang JX, Van Dyke ME, Nicoletta DP (2010) Correlation of cell strain in single osteocytes with intracellular calcium, but not intracellular nitric oxide, in response to fluid flow. *J Biomech* 43(8):1560–1564
162. Schneider P, Ruffoni D, Larsson D, Chiapparini I, Müller R (2012) Image-based finite element models for the investigation of osteocyte mechanotransduction. *J Biomech* 45(1): S436
163. Cardoso L, Fritton SP, Gailani G, Benalla M, Cowin SC (2013) Advances in assessment of bone porosity, permeability and interstitial fluid flow. *J Biomech* 46(2):253–265
164. Marotti G (1990) The original contributions of the scanning electron microscope to the knowledge of bone structure. In: Bonucci E, Motta PM (eds) *Ultrastructure of skeletal tissues SE – 2*, vol 7. Springer, pp 19–39
165. Kerschnitzki M, Wagermaier W, Liu Y, Roschger P, Duda GN, Fratzl P (2011) Poorly ordered bone as an endogenous scaffold for the deposition of highly oriented lamellar tissue in rapidly growing ovine bone. *Cells Tissues Organs* 194(2–4):119–123
166. Sharma D, Ciani C, Marin PAR, Levy JD, Doty SB, Fritton SP (2012) Alterations in the osteocyte lacunar-canalicular microenvironment due to estrogen deficiency. *Bone* 51(3):488–497
167. Kerschnitzki M, Kollmannsberger P, Burghammer M, Duda GN, Weinkamer R, Wagermaier W, Fratzl P (2013) Architecture of the osteocyte network correlates with bone material quality. *J Bone Miner Res* 28(8):1837–1845
168. Varga P, Hesse B, Langer M, Schrof S, Männicke N, Suhonen H, Pacureanu A, Pahr D, Peyrin F, Raum K (2015) Synchrotron x-ray phase nano-tomography-based analysis of the lacunar-canalicular network morphology and its relation to the strains experienced by osteocytes in situ as predicted by case-specific finite element analysis. *Biomech Model Mechanobiol* 14(2):267–282
169. McNamara LM, Majeska RJ, Weinbaum S, Friedrich V, Schaffler MB (2009) Attachment of osteocyte cell processes to the bone matrix. *Anat Rec* 292(3):355–363
170. Wu D, Ganatos P, Spray DC, Weinbaum S (2011) On the electrophysiological response of bone cells using a Stokesian fluid stimulus probe for delivery of quantifiable localized picoNewton level forces. *J Biomech* 44(9):1702–1708
171. Weiner S, Traub W (1992) Bone structure: from angstroms to microns. *FASEB J* 6(3):879–885
172. Parfitt AM (2003) Misconceptions (3): calcium leaves bone only by resorption and enters only by formation. *Bone* 33(3):259–263
173. Marenzana M, Shipley AM, Squitiero P, Kunkel JG, Rubinacci A (2005) Bone as an ion exchange organ: evidence for instantaneous cell-dependent calcium efflux from bone not due to resorption. *Bone* 37(4):545–554
174. Pirklbauer M, Mayer G (2011) The exchangeable calcium pool: physiology and pathophysiology in chronic kidney disease. *Nephrol Dial Transplant* 26(8):2438–2444
175. Talmage RV, Mobley HT (2008) Calcium homeostasis: reassessment of the actions of parathyroid hormone. *Gen Comp Endocrinol* 156(1):1–8
176. Atkins GJ, Findlay DM (2012) Osteocyte regulation of bone mineral: a little give and take. *Osteoporos Int* 23(8):2067–2079
177. Hunter GK, Hauschka PV, Poole AR, Rosenberg LC, Goldberg HA (1996) Nucleation and inhibition of hydroxyapatite formation by mineralized tissue proteins. *Biochem J* 317 (Pt 1):59–64
178. Nakashima T, Hayashi M, Fukunaga T, Kurata K, Oh-Hora M, Feng JQ, Bonewald LF, Kodama T, Wutz A, Wagner EF, Penninger JM, Takayanagi H (2011) Evidence for osteocyte regulation of bone homeostasis through RANKL expression. *Nat Med* 17(10): 1231–1234

179. Feng JQ, Clinkenbeard EL, Yuan B, White KE, Drezner MK (2013) Osteocyte regulation of phosphate homeostasis and bone mineralization underlies the pathophysiology of the heritable disorders of rickets and osteomalacia. *Bone* 54(2):213–221
180. Bélanger LF, Bélanger C, Semba T (1967) Technical approaches leading to the concept of osteocytic osteolysis. *Clin Orthop Relat Res* 54:187–196
181. Blaber EA, Dvorochkin N, Lee C, Alwood JS, Yousuf R, Pianetta P, Globus RK, Burns BP, Almeida EAC (2013) Microgravity induces pelvic bone loss through osteoclastic activity, osteocytic osteolysis, and osteoblastic cell cycle inhibition by CDKN1a/p21. *PLoS One* 8(4), e61372
182. Lane NE, Yao W, Balooch M, Nalla RK, Balooch G, Habelitz S, Kinney JH, Bonewald LF (2006) Glucocorticoid-treated mice have localized changes in trabecular bone material properties and osteocyte lacunar size that are not observed in placebo-treated or estrogen-deficient mice. *J Bone Miner Res* 21(3):466–476
183. Tommasini SM, Trinward A, Acerbo AS, De Carlo F, Miller LM, Judex S (2012) Changes in intracortical microporosities induced by pharmaceutical treatment of osteoporosis as detected by high resolution micro-CT. *Bone* 50(3):596–604
184. Qing H, Bonewald LF (2009) Osteocyte remodeling of the perilacunar and pericanalicular matrix. *Int J Oral Sci* 1(2):59–65
185. Rubin MA, Rubin J, Jasiuk I (2004) SEM and TEM study of the hierarchical structure of C57BL/6J and C3H/HeJ mice trabecular bone. *Bone* 35(1):11–20